



Constructing fast charge separation of $\text{ZnIn}_2\text{S}_4 @\text{CuCo}_2\text{S}_4$ p-n heterojunction for efficient photocatalytic hydrogen energy recovery from quinolone antibiotic wastewater

Ruobing Wang, Weili Yu, Ningjie Fang*, Peng Wang, Yinghao Chu, Shilin Wu, Juan Liang

College of Architecture and Environment, Sichuan University, Chengdu 610065, Sichuan, China



ARTICLE INFO

Keywords:

Photocatalytic hydrogen evolution
Quinolone antibiotic degradation
Synergistic
 $\text{ZnIn}_2\text{S}_4 @\text{CuCo}_2\text{S}_4$
P-n heterojunction

ABSTRACT

Dual-functional catalysts can realize effective photocatalysis for synergistic water remediation and H_2 production by coupling reduction and oxidation reaction in one water-pollutant system. In this work, a novel $\text{ZnIn}_2\text{S}_4 @\text{CuCo}_2\text{S}_4$ nanoflower-like p-n heterojunction catalyst was successfully synthesized by a simple method and used for hydrogen generation from quinolone antibiotic wastewater. $\text{ZnIn}_2\text{S}_4 @\text{CuCo}_2\text{S}_4$ exhibited high hydrogen production activity of $0.36 \text{ mmol}\cdot\text{g}^{-1}\cdot\text{h}^{-1}$ in ofloxacin (OFL) solution. Simultaneously, the OFL removal efficiency and mineralization rate were up to 89.4 % and 92.24 %, respectively. The interface charge transfer mechanism was thoroughly investigated through systematic characterizations and DFT calculations. The results show that CuCo_2S_4 addition significantly improved the separation and transfer rate of photoinduced carriers. Additionally, the possible degradation pathways of OFL were analyzed using LC-MS. This study provides a new approach for simultaneous energy conversion and environmental pollution treatment, offering a new pathway for achieving sustainable energy development through the management of antibiotic wastewater.

1. Introduction

Quinolone antibiotics exhibits stable chemical structure and difficulty in biodegradation and has been detected with varying degrees in groundwater, surface water, wastewater treatment plants and so on [1–6]. Conventional wastewater treatment processes are unable to effectively remove quinolone antibiotics. Advanced oxidation technologies exhibit good removal efficacy, but the treatment process is complex, with high consumption of oxidants and high treatment costs [7]. Besides, developing clean and green energy (such as hydrogen) to replace fossil fuels is a feasible path towards addressing environmental pollution and energy crisis [8–10]. Photocatalysis technology has been widely applied in photocatalytic hydrogen production and organic compound degradation due to its energy-efficient and environment-friendly characteristics [11–13]. However, in conventional photocatalytic hydrogen production systems, a large number of expensive and toxic sacrificial agents is added to facilitate hydrogen generation. In the coupled photocatalysis system for synergistic water remediation and H_2 production, the pollutant can serve as electron donors, which is similar to sacrificial agents [14–17]. Therefore, the integration of different photocatalytic fields and the construction of

bifunctional photocatalytic systems are the opportunities and challenges that need to be addressed currently [18–20].

To achieve the synergistic degradation of water pollutants and hydrogen production, the key lies in designing and developing suitable photocatalyst [21,22]. Among various photocatalysts, metal sulfides have become one of the most important semiconductor materials [23–26]. The layered ternary metal sulfide ZnIn_2S_4 has a tunable bandgap ranging from 2.06 to 2.85 eV, in which the conduction band of ZnIn_2S_4 is more negative than the reduction potential of water splitting, while the valence band is more positive than the oxidation potentials of many organic pollutants (tetracycline antibiotics, quinolone antibiotics etc.) [27–29]. Besides, ZnIn_2S_4 possesses large specific surface area, low toxicity, low cost, good chemical stability, and strong visible light absorption ability [30–32]. However, pure ZnIn_2S_4 exhibits low photocatalytic activity due to the rapid recombination of electron-hole pairs. Common modification methods include constructing heterojunctions, elemental doping, morphology control, and so on. Among them, the construction of p-n heterojunction systems with built-in electric fields can effectively promote the separation of photo-generated carriers [33]. He et al. [34] prepared a $\text{CoFe}_2\text{O}_4/g\text{-C}_3\text{N}_4$ p-n heterojunction photocatalyst and showed high photoactivity toward hydrogen evolution and

* Corresponding author.

E-mail address: f nj@scu.edu.cn (N. Fang).

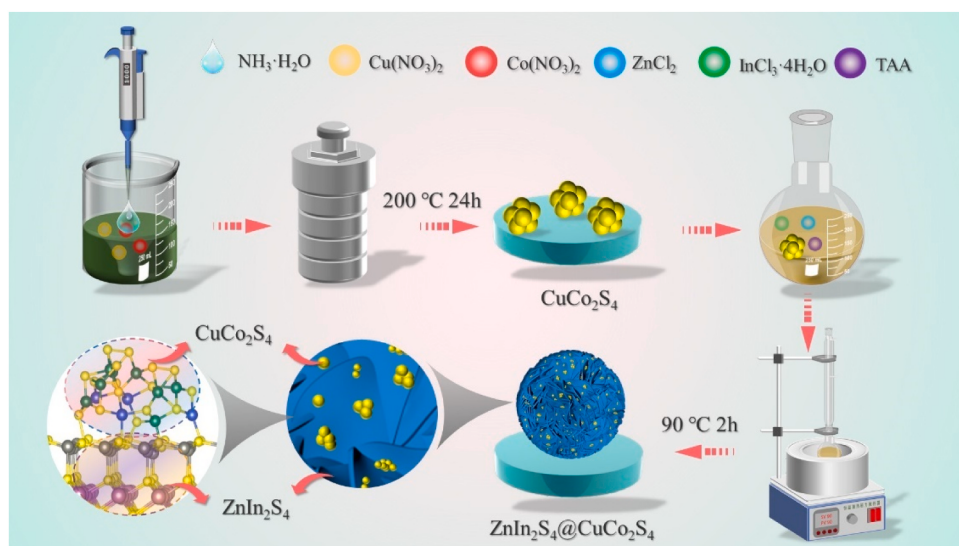


Fig. 1. Synthesis diagram of ZIS@CCS.

antibiotics removal, which can be attributed to its large specific surface area, narrow band gap, and internal electric field at the interface.

CuCo_2S_4 is a ternary metal sulfide with a spinel structure. It exhibits p-type semiconductor characteristics, a narrow band gap structure as well as suitable surface hydrophilicity [35,36]. Its two-dimensional nanostructure ensures that it can tightly associate with the host catalyst, which in return increasing the contact surface area and promoting material exchange and electron transfer [37,38]. For example, Wang et al. [39] developed an effective $\text{CuCo}_2\text{S}_4/\text{Bi}_2\text{WO}_6$ catalyst. The CuCo_2S_4 addition broadens the light responsive range and facilitates the separation and transfer of photogenerated carriers. Therefore, the combination of p- CuCo_2S_4 and n- ZnIn_2S_4 to construct p-n heterojunction photocatalysts could potentially be a feasible approach for recovery hydrogen energy from quinolone antibiotic wastewater.

In this work, a novel n- ZnIn_2S_4 @p- CuCo_2S_4 nanoflower-like heterojunction photocatalyst was successfully synthesized by a simple method and used for hydrogen production from quinolone antibiotic wastewater. The most practical and cost-effective ratios for different types of quinolone antibiotics (ofloxacin, lomefloxacin, ciprofloxacin, norfloxacin, and enrofloxacin), different pollutant concentrations and catalyst concentrations were explored. The charge transfer mechanism and potential photodegradation pathway of this coupled system were also discussed. The results demonstrate that the prepared ZnIn_2S_4 @ CuCo_2S_4 can simultaneously produce hydrogen and remove quinolone antibiotics through photocatalysis, with the best hydrogen evolution rate of $0.36 \text{ mmol}\cdot\text{g}^{-1}\cdot\text{h}^{-1}$ in ofloxacin solution. Besides, the removal efficiency and the total organic carbon mineralization rate of ofloxacin reach up to 89.35 % and 92.24 %, respectively. This work provides a new avenue for simultaneous removal of organic pollutants and synchronous generation of green energy from wastewater treatment, which is beneficial for the resolution of environmental pollution and energy crises.

2. Experimental section

2.1. Chemicals and reagents

Zinc chloride (ZnCl_2), Indium (III) chloride tetrahydrate ($\text{InCl}_3\cdot 4\text{H}_2\text{O}$), Thioacetamide (CH_3CSNH_2 , TAA), Copper (II) nitrate trihydrate ($\text{Cu}(\text{NO}_3)_2\cdot 3\text{H}_2\text{O}$), Cobalt nitrate hexahydrate ($\text{Co}(\text{NO}_3)_2\cdot 6\text{H}_2\text{O}$), Thiourea (H_2NCSNH_2), Ammonia solution ($\text{NH}_3\cdot\text{H}_2\text{O}$), Glycerol ($\text{C}_3\text{H}_8\text{O}_3$) and Triethanolamine ($\text{C}_6\text{H}_{15}\text{NO}_3$, TEOA) were of analytical grade and used without further purification.

2.2. Synthesis of CuCo_2S_4 (CCS)

Firstly, 1 mmol $\text{Cu}(\text{NO}_3)_2\cdot 3\text{H}_2\text{O}$ and 2 mmol $\text{Co}(\text{NO}_3)_2\cdot 6\text{H}_2\text{O}$ were dissolved into 30 mL of deionized water. After stirring for 10 min, 4 mmol of thiourea and 2.5 mL of ammonia were added to the solution under constant stirring. The obtained solution was transferred into a 100-mL Teflon-lined autoclave and maintained at 200 °C for 24 h. After cooling down to room temperature, the samples were washed five times with deionized water and anhydrous ethanol solution and dried at 60 °C overnight.

2.3. Synthesis of ZnIn_2S_4 @ CuCo_2S_4 (ZIS@CCS)

Typically, a certain amount of CCS was dissolved in a mixed solution of 40 mL water and 10 mL glycerol. After that, 0.5 mmol of ZnCl_2 , 1 mmol of $\text{InCl}_3\cdot 4\text{H}_2\text{O}$ and 4 mmol of TAA were added to the above suspension. Following this, the resulting mixture was transferred into an oil bath and heated to reflux at 90 °C for 2 h under strong stirring. After cooling down to room temperature, the final product was washed by five times with deionized water and anhydrous ethanol solution and dried at 60 °C overnight.

For comparison, pure ZnIn_2S_4 (ZIS) was synthesized by the same process, just without the addition of CuCo_2S_4 (CCS) (Fig. 1). The as-synthesized samples with 5 wt%, 7.5 wt%, 10 wt%, 12.5 wt% and 15 wt% CuCo_2S_4 loading amount were labeled as ZnIn_2S_4 @ CuCo_2S_4 -5 (ZIS@CCS-5), ZnIn_2S_4 @ CuCo_2S_4 -7.5 (ZIS@CCS-7.5), ZnIn_2S_4 @ CuCo_2S_4 -10 (ZIS@CCS-10), ZnIn_2S_4 @ CuCo_2S_4 -12.5 (ZIS@CCS-12.5), and ZnIn_2S_4 @ CuCo_2S_4 -15 (ZIS@CCS-15), respectively. The practical content of CCS in ZIS@CCS-7.5 was detected as 7.11 % (Table S1).

2.4. Characterization

The crystal structures of the samples were analyzed by X-ray diffraction (XRD, Rigaku Ultima IV, Japan). Microstructure and morphology information were examined by scanning electron microscopy (SEM, Hitachi, Japan) and transmission electron microscopy (TEM, FEI Titan G2 60–300). The Energy dispersive spectroscopy (EDS) of samples were also investigated during the SEM measurement. The UV-vis diffuse reflectance spectra which was analyzed by a spectrophotometer (DRS, UV-2600, Shimadzu, Japan) with a wavelength range of 200–800 nm. Photoluminescence spectra (PL, Hitachi, F-7100, Japan) were used to characterize Steady-state photoluminescence in all the samples. The chemical compositions and surface states were

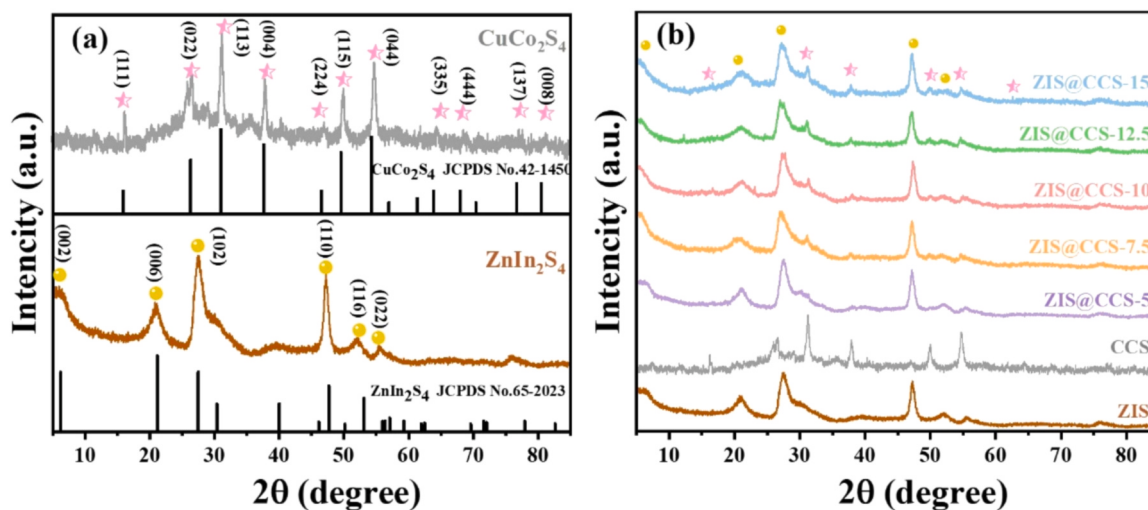


Fig. 2. XRD images of different samples.

demonstrated using X-ray photoelectron spectroscopy (XPS, Thermo Fisher Scientific Escalab250Xi, with a monochromatic Al K X-ray source). The specific surface areas of the catalysts were determined by applying the Brunauer Emmett Teller (BET) method to the adsorption of nitrogen at 393 K. Photoelectrochemical measurements were monitored by a CHI660E electrochemical station with a standard three-electrode system. The electrolyte was a 0.5 M Na₂SO₄ solution.

2.5. Photocatalytic performance test

H₂ production experiments were performed in a CEL-PAEM-D8 photocatalytic reactor which was connected to a closed gas circulation system while irradiated with a 300 W Xe lamp (CEL-PE3⁰⁰E-³A, Beijing). In a typical method, the photocatalyst (10 mg) was suspended in a reaction cell containing 50 mL of a mixed solution of 10 vol% TEOA. Before irradiation, the reaction system was vacuumed for 30 min to remove residual gases. The reactant solution was maintained at 6 °C by a flow of cooling water during the reaction. The hydrogen gas produced was detected by gas chromatography (GC9720, TCD detector, Ar carrier, Beijing) every 1 h.

The TEOA as an electron donor was replaced with different organic pollutants, and the reaction conditions were the same as above. Before irradiation, the reaction system was vacuumed to remove residual gases and maintained in the dark for 30 min to reach adsorption equilibrium. The concentration of organic pollutant was determined with high-performance liquid chromatography (HPLC, LC-100, Shanghai), equipped with a C18 column (Agilent ZORBAX SB-C18, 5 μm, 4.6 mm × 250 mm). The removal percent (η) was calculated by η (%) = (1 - C/C₀) × 100 %, where C₀ and C are the concentration of pollutants before and after the reaction, respectively.

The measurement of apparent quantum yield (AQY) follows the same conditions as the photocatalytic testing. The difference lies in the Xenon lamp being equipped with specific bandpass filters to obtain the desired monochromatic incident wavelength (313 nm, 365 nm, 400 nm or 450 nm). AQY is approximately calculated using the following equation [40,41]:

$$AQY = \frac{2 \times \text{the number of evolved hydrogen molecules}}{\text{the number of incident photons}} \times 100\%$$

To explore the mechanism of the photocatalyst degradation under the coupled system, BQ, IPA and TEOA were selected as the scavengers of O₂·OH and h⁺, respectively.

2.6. DFT calculations

The DFT calculations were carried out using Vienna Ab Initio Simulation Package (VASP 5.4). The pseudo potential was implemented by Perdew–Burke–Ernzerhof (PBE) [42]. The projected augmented wave (PAW) was used to describe ion–electron interaction. The ZnIn₂S₄ (001) with 112 atoms was selected as slab model [43]. The cut-off energy and K points were 450 eV and 3 × 3 × 1, respectively. The vacuum layer was 20 Å. The structure optimization was relaxed until the final force on each atom was less than – 0.02 eV/Å.

3. Results and discussion

3.1. Characterization

The crystal structures and phase compositions of ZnIn₂S₄, CuCo₂S₄, and ZIS@CCS were preliminarily evaluated through X-ray diffraction (XRD) analysis (Fig. 2). A comparison of ZnIn₂S₄ with the standard card revealed characteristic peaks at 2θ = 7.15°, 21.4°, 27.6°, 47.1°, 52.4° and 55.7°, which corresponds to the (002), (006), (102), (110), (116) and (022) planes of the hexagonal phase ZnIn₂S₄ (JCPDS, No. 65–2023), respectively [44]. The absence of offset peaks and impurity peaks indicates the successful synthesis of pure hexagonal-phase ZIS. Similarly, CuCo₂S₄ exhibited good agreement with the standard card (JCPDS, No. 42–1450), indicating high crystallinity [45]. The ZIS@CCS samples retained the characteristic peaks of hexagonal-phase ZnIn₂S₄, indicating the preservation of its structural integrity and crystallinity. This suggests that the addition of CCS does not affect the ZIS phase. Although some diffraction peaks of CuCo₂S₄ were masked, they can still be identified in the graph, likely due to the low content and high dispersion of CuCo₂S₄ in the composite.

To obtain information on the morphology and microstructure of ZIS, CCS, and ZIS@CCS, scanning electron microscopy (SEM) and transmission electron microscopy (TEM) were employed. The SEM (Fig. 3a) and TEM (Fig. S1c) images of ZIS revealed a flower-like spherical structure composed of intersecting nanosheets with particle diameters of approximately 1–2 μm. The CCS, on the other hand, consisted of small particles in the range of 100–200 nm, which leads to the formation of nanoclusters and further aggregated into cloud-like assemblies (Fig. S1a–b). The results after the in-situ growth of ZIS on CCS (Fig. 3b and Fig. S1d) showed that the stacked CCS was dispersed into small nanoclusters during the formation of ZIS, which then adhered to the 2D layers of ZIS. This demonstrated the successful synthesis of the ZIS@CCS material. In AFM image (Fig. 3e–f), the thickness of the layer can be

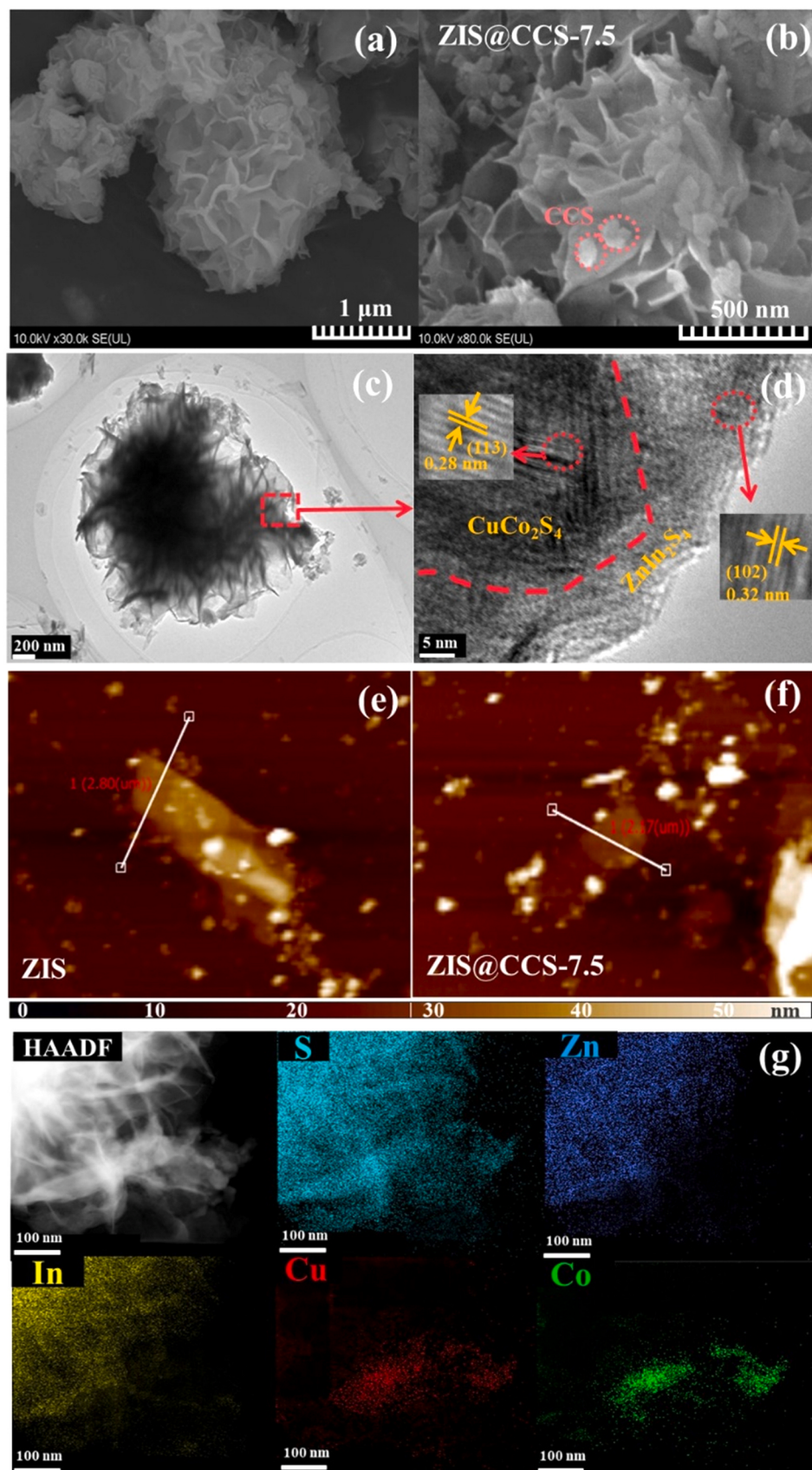


Fig. 3. SEM images of (a) ZIS, (b) ZIS@CCS-7.5; TEM images of (c) ZIS@CCS-7.5; (d) HRTEM image of ZIS@CCS-7.5; AFM images of (e) ZIS and (f) ZIS@CCS-7.5; and (g) high-magnification TEM-EDS mappings of ZIS@CCS-7.5.

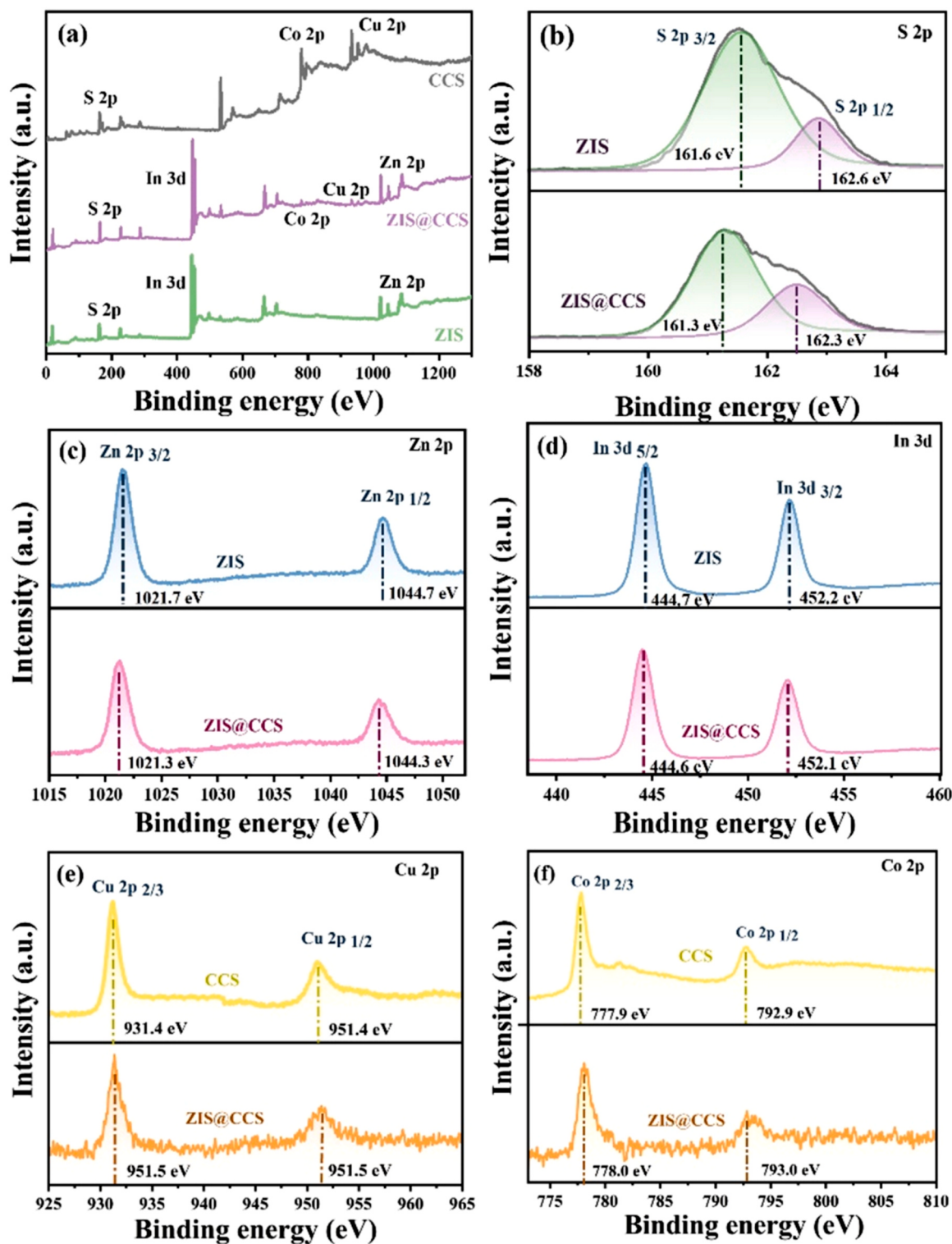


Fig. 4. (a) The survey XPS spectra of different samples and XPS high-resolution scans of (b) S 2p, (c) Zn 2p, (d) In 3d, (e) Cu 2p, and (f) Co 2p.

determined from the depth of the color. The deeper the color, the less the thickness. It was also observed that the nanosheets of ZIS became thinner and exhibited a more diverse and slightly reduced flower-like morphology after the addition of CCS. The diameter of the flower-like structure decreased to approximately 0.5–1 μm .

High-resolution transmission electron microscopy (HRTEM) images of ZIS and CCS displayed clear lattice fringes (Fig. 3c-d). Fig. 3d provides detailed information about the internal structure of the ZIS@CCS

nanocomposite. The left cluster with a plane spacing of 0.28 nm corresponds to the (113) crystal plane of CCS, while the right thin-layered structure with a spacing of 0.32 nm is attributed to the (102) crystal plane of hexagonal ZIS. A clear intimate contact interface between CCS and ZIS was observed, which would facilitate the efficient transfer of photogenerated charge carriers between them. The spatial distribution of elements in ZIS@CCS was characterized by high-magnification TEM-EDS analysis in Fig. 3g and Fig. S3. The analysis revealed that S, Zn, In,

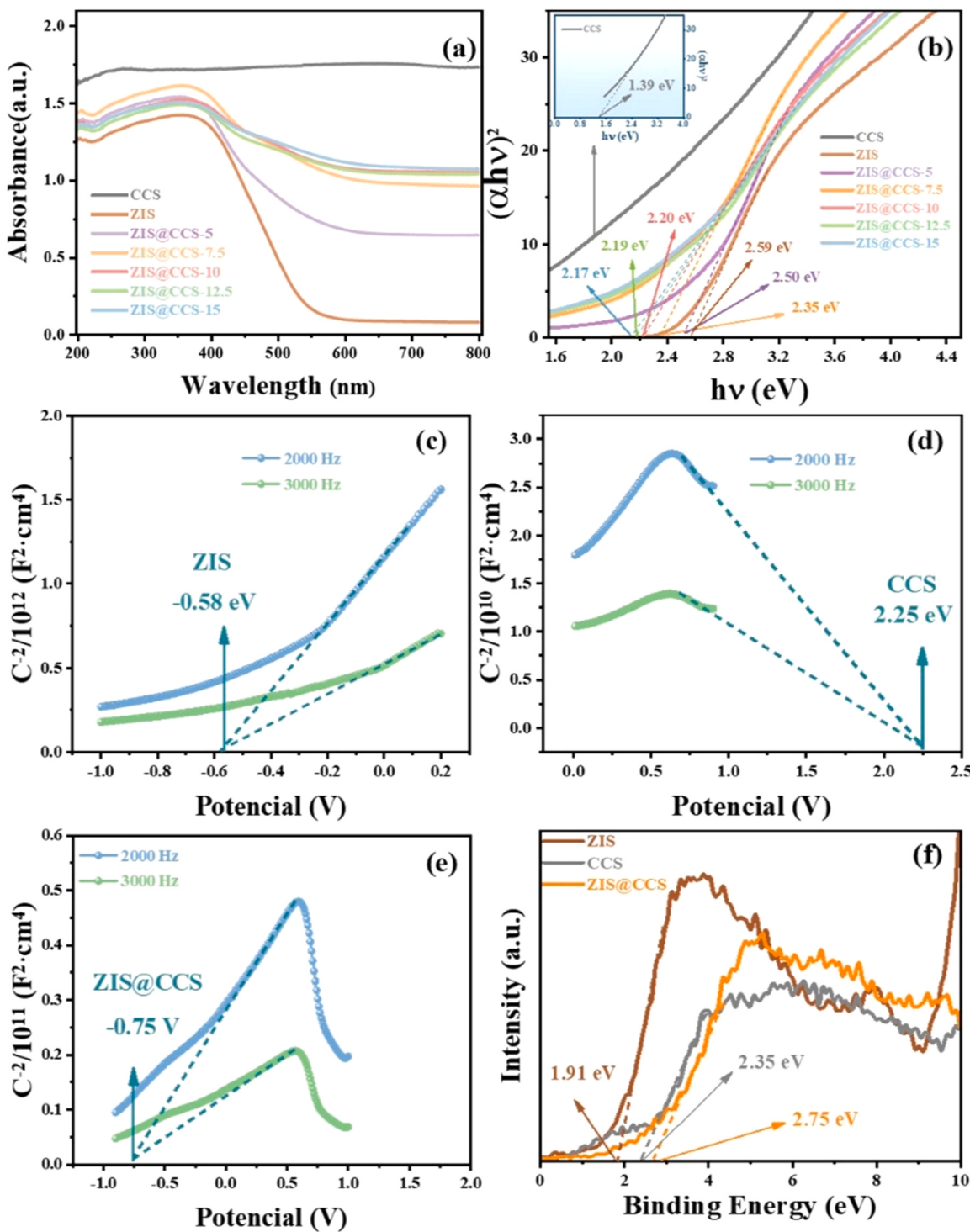


Fig. 5. (a) UV-vis spectra and (b) the plots of the transformed Kubelka–Munk function versus the light energy. Mott–Schottky plot of (c) ZIS, (d) CCS and (e) ZIS@CCS-7.5. (f) VB XPS spectra of ZIS, CCS, and ZIS@CCS-7.5.

Cu, and Co elements are uniformly distributed throughout the particles, and there is a clear distinction between the regions corresponding to ZIS and CCS, indicating the successful synthesis of ZIS@CCS.

X-ray photoelectron spectroscopy (XPS) was employed to analyze the surface composition and chemical valence states of ZIS, CCS, and ZIS@CCS catalysts. The XPS spectra of ZIS@CCS clearly showed peaks corresponding to S, In, and Zn elements, with Cu and Co peaks being smaller but still discernible. This suggests the successful formation of ZIS@CCS (Fig. 4a). As shown in Fig. 4b, the S 2p spectrum of ZIS

exhibited two peaks at 161.6 and 162.6 eV, corresponding to the S 2p_{3/2} and S 2p_{1/2} states, respectively. In the case of ZIS@CCS, the S 2p peaks slightly shifted to lower binding energies, appearing at 161.3 and 162.3 eV, respectively. This shift can be attributed to the electron transfer between the S atoms in ZIS and CCS [46]. The two peaks in the Zn 2p spectrum of pure ZIS corresponded to Zn 2p_{3/2} and Zn 2p_{1/2}, while the two peaks in the In 3d spectrum corresponded to In 3d_{5/2} and In 3d_{3/2}, respectively, indicating the presence of Zn²⁺ and In³⁺ cations [47]. Likewise, the Cu 2p and Co 2p spectrum of CCS corresponded to Cu

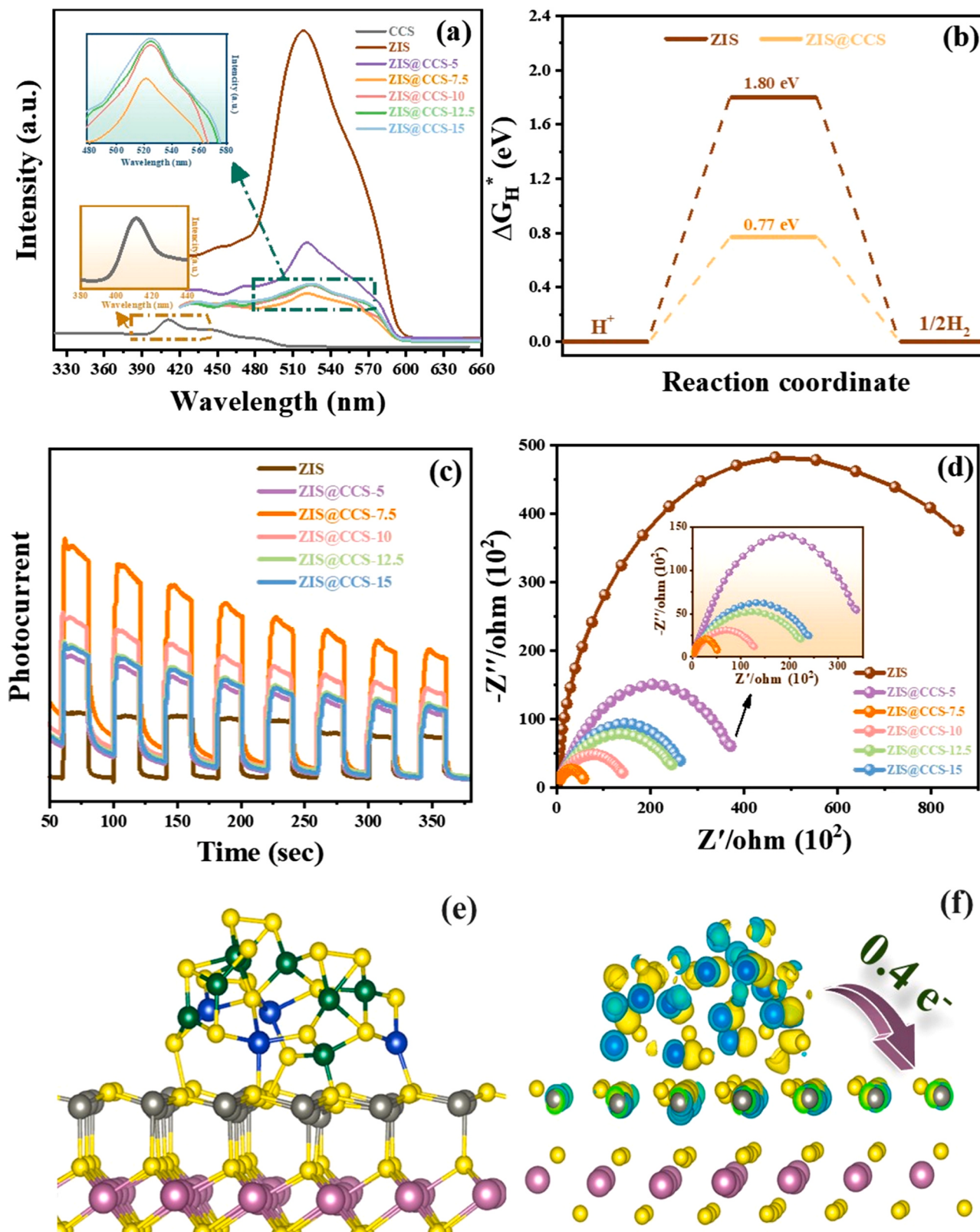


Fig. 6. (a) PL spectra of different samples. (b) Calculated ΔG_H^* diagrams for photocatalytic H_2 production of modeled ZIS and ZIS@CCS (c) Transient photocurrent spectra (d) EIS spectra of different samples (e) The corresponding atomic model for ZIS@CCS (f) The planar averaged charge density difference for the ZIS@CCS model, the yellow and blue regions represent the consumption and accumulation of electrons. (yellow-S, gray-Zn, pink-In, blue-Cu, green-Co).

$2p_{3/2}$, Cu $2p_{1/2}$, Co $2p_{3/2}$, and Co $2p_{1/2}$, respectively, indicating the presence of Cu^{2+} and Co^{2+} ions [37]. After the combination of ZIS and CCS, the Zn 2p and In 3d spectra of ZIS@CCS exhibited negative positive shifts, while the Cu 2p and Co 2p spectra showed noticeable shifts. These results can be attributed to the strong electronic interaction between ZIS and CCS, confirming changes in electron density and charge transfer at the interfaces. Considering the direction of binding energy shift for S atoms and metals, the overall electron transfer direction is from the CCS surface to ZIS.

The nitrogen adsorption-desorption isotherms (Fig. S4a) revealed that CCS exhibited a typical type II isotherm, indicating the existence of multilayer dispersed structure. The ZIS and ZIS@CCS composite photocatalysts showed mixed I/IV type isotherms with hysteresis loops, closing at a relative pressure of $P/P_0 = 0.4$. This phenomenon indicates that ZIS@CCS possesses a hierarchical porous structure with micro- and meso-pores. The pore size distribution (Fig. S4b) demonstrated that ZIS@CCS retained some of the micro-pores of ZIS and exhibited a hierarchical pore structure, which was favorable for material transportation and transfer. Furthermore, the specific surface area of ZIS@CCS ($31.96\text{ m}^2/\text{g}$) was lower than that of pure ZIS ($77.26\text{ m}^2/\text{g}$), indicating that CCS successfully anchored on the ZIS surface and occupied a portion of the pores. However, Fig. 7a-b showed that the hydrogen production activity of ZIS@CCS was significantly higher than that of ZIS, indicating that the BET surface area is not the key factor influencing the photocatalytic activity.

Fig. S4(c-d) analyzes and evaluates the composition of the surface chemistry of the material using FTIR. As shown in Fig. S4d, two peaks at 1610 cm^{-1} and 1396 cm^{-1} corresponding to the surface absorbed water molecules and hydroxyl groups are observed over $ZnIn_2S_4$ [48]. Furthermore, the bending vibrations of Cu-S and Co-S stretching modes depicted two distinct peaks at 1123 cm^{-1} and 856 cm^{-1} in the spectrum of $CuCo_2S_4$ [49]. After the formation of the composite, the position and intensity of the peaks may undergo varying degrees of change. Compared to ZIS and CCS, ZIS@CCS retained the characteristic peaks of the two pure-phase materials. Furthermore, the position of characteristic peaks shifts towards shorter wavelengths, indicating the occurrence of interactions between ZIS and CCS [50]. The hydrophilicity or hydrophobicity of the catalyst surface can be directly observed through the measurement of the static water contact angle (CA). From the water contact angle in Fig. S5, the CA of ZIS, CCS and ZIS@CCS were determined to be 0.000, indicating strong water wetting properties and superhydrophilicity of the composite surface [51].

3.2. Photocatalytic activity and photoelectrochemical properties

The optical properties of ZIS, CCS, and ZIS@CCS were studied using UV-visible absorption spectroscopy, as shown in Fig. 5a-b. Compared to ZIS and CCS, the ZIS@CCS composite material exhibited enhanced light absorption in the wavelength range of 200–800 nm. The absorption edge of pure-phase ZIS was located at 532 nm, corresponding to a bandgap energy of 2.59 eV, while the bandgap energy of CCS was 1.39 eV. Upon the combination of ZIS and CCS, the absorption intensity increased significantly and there was a redshift. The addition of narrow bandgap CCS induces a significant photoresponse, broadening the range of light absorption, and also reduces the bandgap of the composite material, thus promoting its absorption of visible light [52–54]. Based on the UV-visible absorption spectra and the equation $(\alpha h\nu)^2 = A(h\nu - E_g)^n$ [55], the bandgap energies of the ZIS@CCS series were calculated to be 2.50, 2.35, 2.20, 2.19 and 2.17 eV, respectively, with the bandgap width decreasing as the concentration of CCS increased.

To further elucidate the flat band positions of the catalyst, Mott-Schottky analysis was performed to determine the positions of the conduction band (CB) and valence band (VB) for each component in the material (Fig. 5c-d). The curve obtained for ZIS exhibited a positive slope, consistent with the behavior of a typical n-type semiconductor, with a flat band potential of -0.58 eV (vs. Ag/AgCl). On the other hand,

CCS acted as a p-type semiconductor, with a negative slope and a flat band potential of 2.25 eV (vs. Ag/AgCl). The E_{fb} values for n-type and p-type semiconductors can be converted into the standard hydrogen electrode (NHE) potential [56,57]. Thus, the E (vs. NHE) values for ZIS and CCS are estimated to be -0.38 eV and 2.05 eV , respectively. As shown in the Fig. 5e, the E (vs. NHE) value of the ZIS@CCS composite material exhibits a shift, indicating an increased band edge curvature. This is beneficial for the separation and transfer of photo-generated charge carriers. Since the E (vs. NHE) value for an n-type semiconductor is typically 0.3 eV higher than the CB and the E (vs. NHE) value for a p-type semiconductor is typically 0.3 eV lower than the VB, the estimated CB value for ZIS is around -0.68 eV , while the estimated VB value for CCS is around 2.35 eV [58]. Additionally, through VB-XPS analysis (Fig. 5f), it can be visually observed that the VB of ZIS is 1.91 eV and the VB of CCS is 2.35 eV . When n-type ZIS comes into contact with p-type CCS, the large difference in Fermi energy levels causes the fast transfer of electrons from CCS to ZIS and holes to transfer from ZIS to CCS until the two Fermi energy levels reach equilibrium.

When the excitation wavelength is 400 nm , the photoluminescence (PL) emission spectra of different synthesized samples were monitored for a clear comparison of their optical properties. Fig. 6a shows the photoluminescence spectra, which indicates a significant decrease in the PL intensity of the catalyst after adding CCS compared to ZIS. This decrease in PL intensity suggests a reduction in the recombination rate of photoexcited carriers, with the peak intensity of ZIS@CCS-7.5 being the lowest, indicating the highest carrier separation efficiency. Fig. 6b further elucidates the performance of the catalyst for the hydrogen evolution reaction (HER) based on density functional theory (DFT) calculations. Both the ZIS and ZIS@CCS models exhibit positive hydrogen adsorption energies, indicating that hydrogen desorption is more favorable kinetically than hydrogen adsorption [59–61]. The ΔG_H^* value of ZIS@CCS (0.77 eV) is much smaller than that of ZIS (1.80 eV), suggesting that the reaction barrier for hydrogen gas generation is lower in ZIS@CCS, indicating superior HER performance [62]. To validate the enhanced photogenerated carrier transfer characteristics of ZIS@CCS, transient photocurrent responses were measured under several cycles of light irradiation, as shown in Fig. 6c. The rapid transient response of the photocurrent during the switching of light illumination states implies close contact between the components of the composite material, ZIS@CCS. The photocurrent response of ZIS@CCS is higher than that of pure ZIS. ZIS@CCS-7.5 shows the highest response value, indicating stronger visible light absorption and effective separation of photogenerated charge carriers in the composite material. In addition, the electrochemical impedance spectroscopy (EIS) plots of ZIS and ZIS@CCS are shown in Fig. 6d. Compared to pure ZIS, the arc radius of the photocatalyst after loading CCS is significantly reduced. ZIS@CCS-7.5 has the smallest radius, indicating a lower catalyst resistance and increased separation and transfer of photogenerated charge carriers.

To further investigate the composite structure of ZIS and CCS, we established a theoretical model and used first-principles calculations within the density functional theory (DFT) framework to study their electronic properties [63–65]. ZIS, with a hexagonal structure, exhibits a grouped stacking of S-Zn-S-In-S-In-S layers, with the quadrilateral cluster structure of CCS positioned on top of ZIS. A comparison of the optimized and initial models (Fig. S6) shows that the Cu and Co atoms of CCS actively form bonds with the S atoms of ZIS, indicating electron transfer from CCS to ZIS directionally (Fig. 6e). This finding is consistent with the XPS results. The charge density difference based on DFT calculations (Fig. 6f) further confirms these results. The yellow and blue regions correspond to charge depletion and accumulation, respectively, indicating the migration of electrons with an energy of 0.4 eV from CCS to ZIS at the contact interface (Table S2).

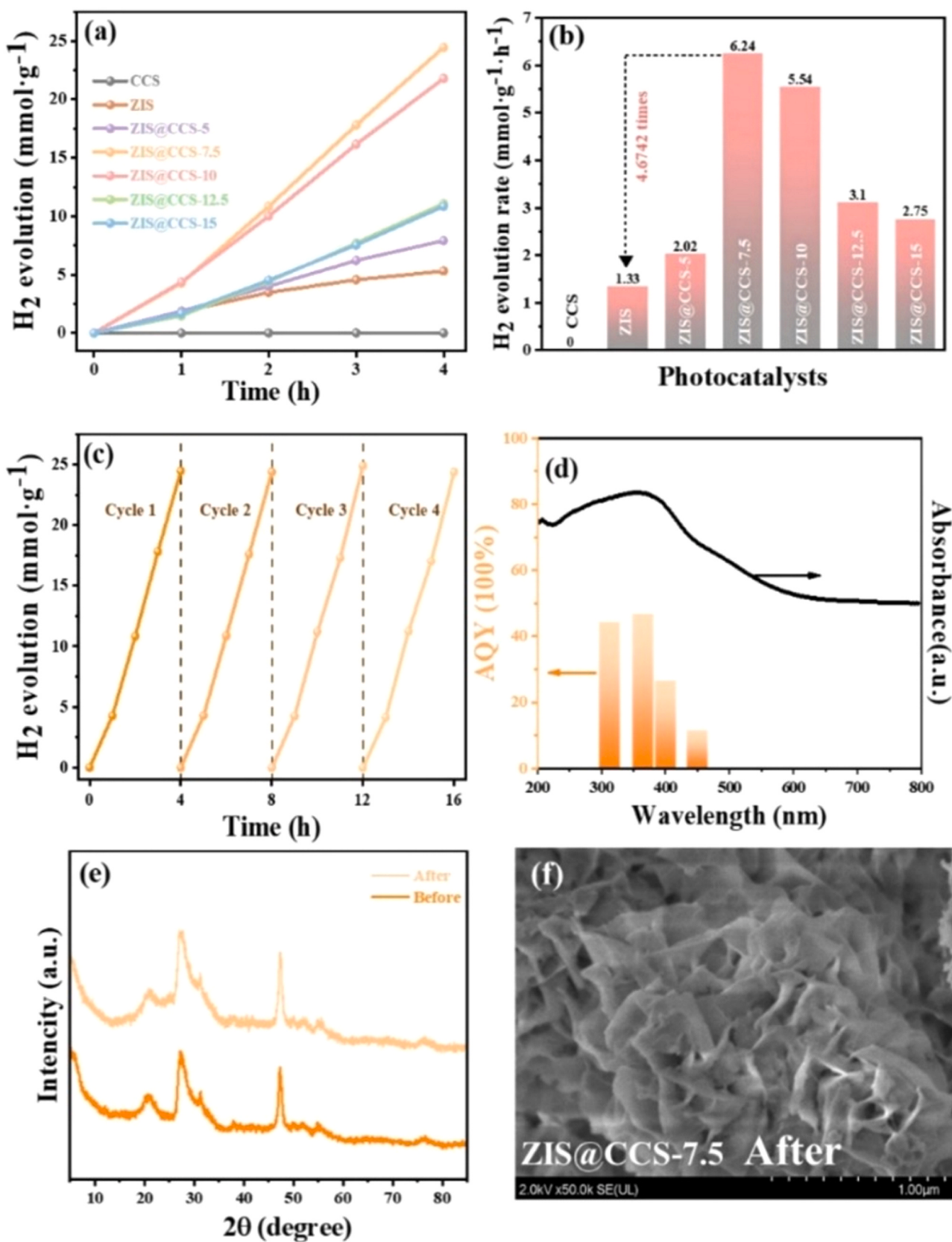


Fig. 7. (a-b) Photocatalytic H_2 evolution over different samples, and (c) cycling stability of ZIS@CCS-7.5; (d) Wavelength-dependent AQY of ZIS@CCS-7.5; (e) XRD image and (f) SEM images of ZIS@CCS-7.5 after four cycles.

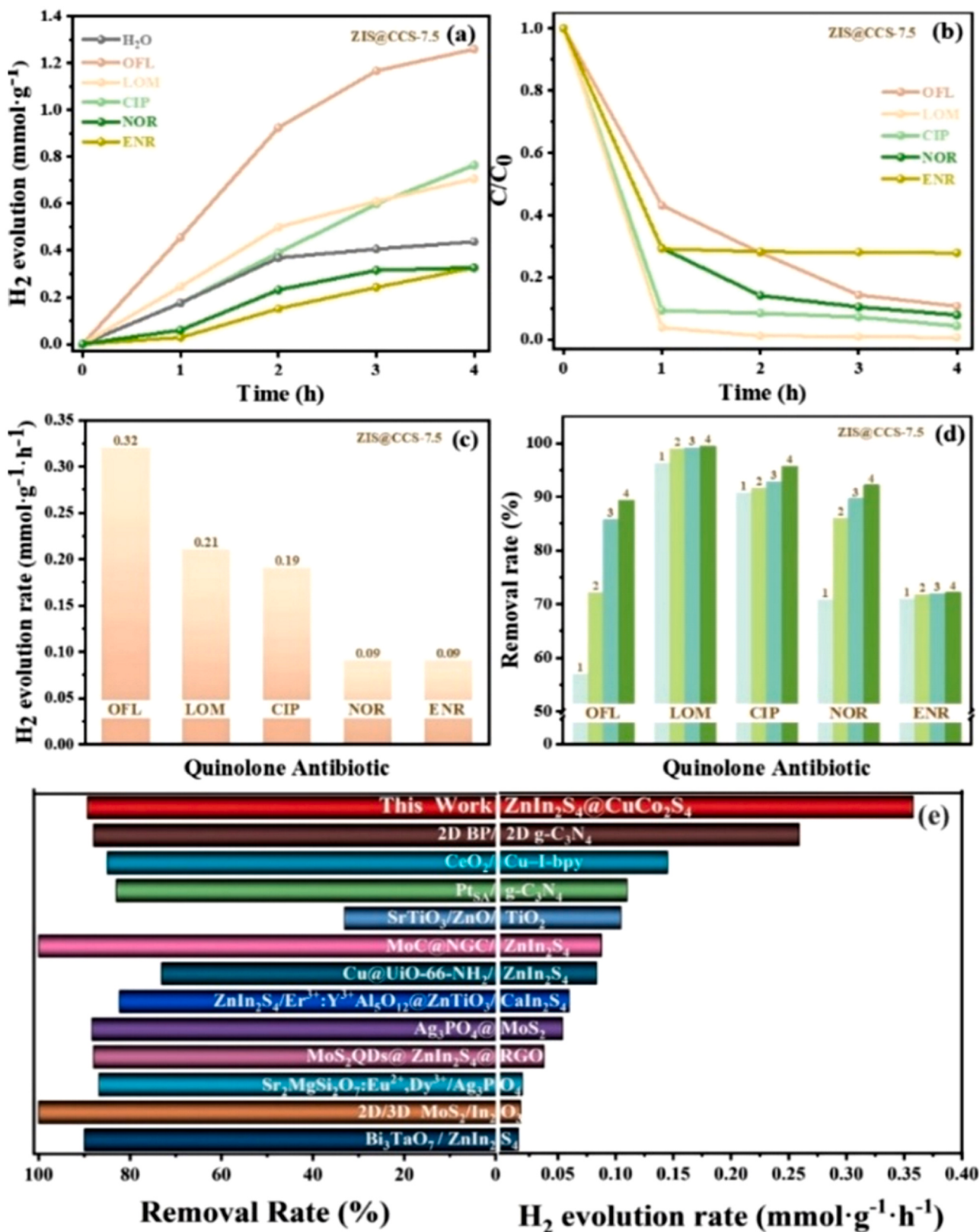


Fig. 8. (a-d) Simultaneous photocatalytic H_2 evolution and the degradation efficiency of different pollutants over ZIS@CCS; (e) Comparison of photocatalytic hydrogen evolution performances and degradation efficiency.

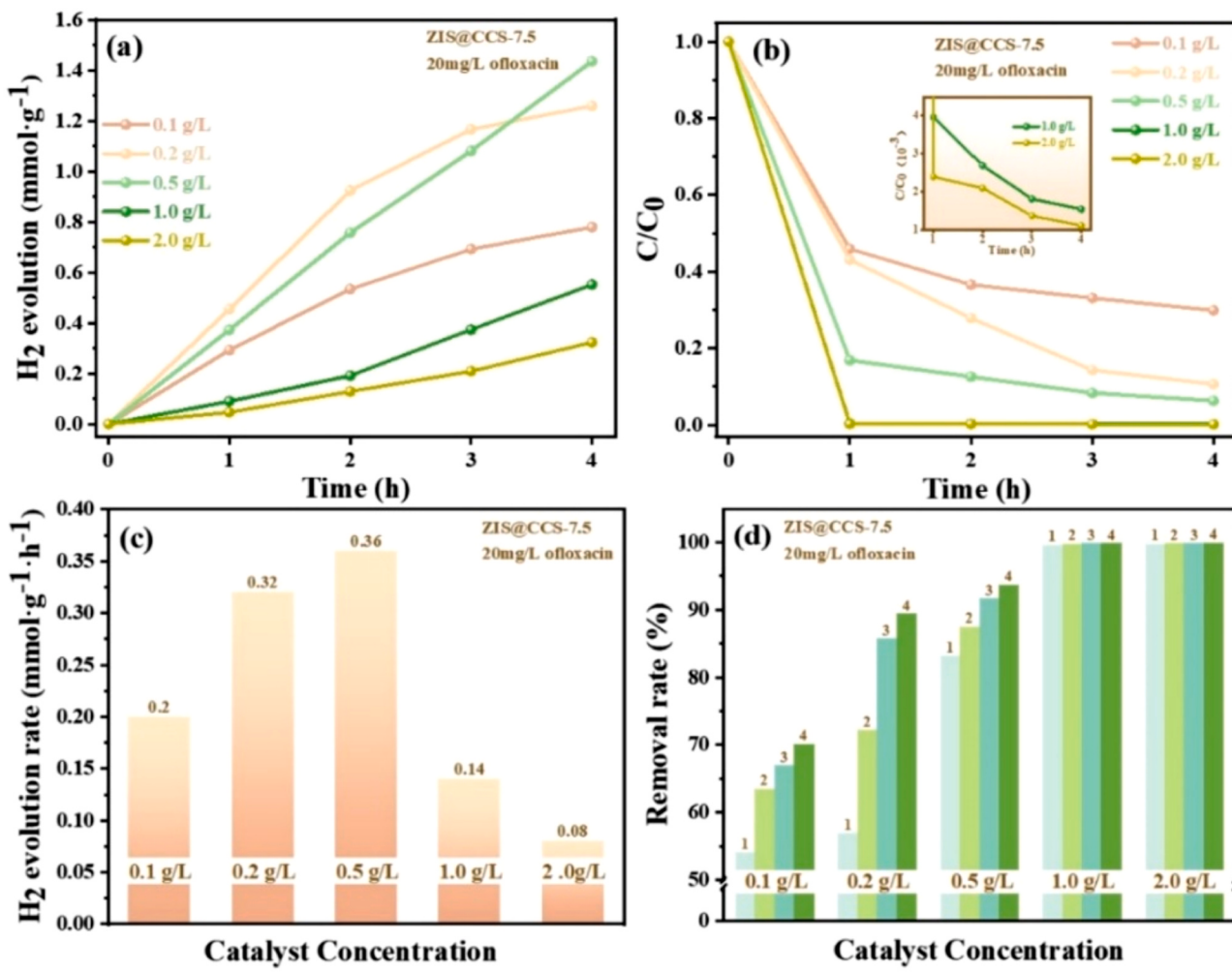


Fig. 9. Simultaneous photocatalytic H₂ evolution rate and the degradation efficiency of OFL over different concentrations of ZIS@CCS.

3.3. Dual photocatalytic activity

To evaluate the photocatalytic activity of the synthesized samples, we compared the photocatalytic hydrogen production performance of each sample using triethanolamine (TEOA) as a sacrificial agent. The results showed that the hydrogen evolution curves of the catalyst exhibited excellent linearity (Fig. 7a-b). Among these, CCS showed no hydrogen evolution activity in triethanolamine, and the hydrogen evolution rate of ZIS was 1.33 mmol·g⁻¹·h⁻¹. With the addition of CCS, the hydrogen evolution rate was improved to varying degrees due to the formation of heterojunctions between ZIS and CCS, which promoted the separation of electron-hole pairs. Among them, the catalyst with a composite ratio of 7.5 wt% CCS showed the best hydrogen evolution activity, reaching up to 6.24 mmol·g⁻¹·h⁻¹, which was 4.67 times higher than that of pure ZIS. This excellent enhancement effect may be due to a more favorable electron transfer pathway, which effectively inhibits electron-hole recombination. From Fig. 7d, it can be observed that the action spectrum of ZIS@CCS-7.5 corresponds well to the ultraviolet-visible absorption spectrum. The AQY values are 44.06 % (at 313 nm), 46.49 % (at 365 nm), 26.44 % (at 400 nm), and 11.34 % (at 450 nm), respectively, indicating that the ZIS@CCS-7.5 photocatalyst possesses excellent light absorption and utilization capabilities. Cycling stability is one of the key factors determining the performance of photocatalysts. In the experiment of four cycles of hydrogen production under continuous reaction of ZIS@CCS-7.5 for 4 h (Fig. 7c), the hydrogen generation rate remained essentially unchanged during the four cycles, and the crystal structure and morphology showed no

obvious changes, indicating good stability and recyclability (Fig. 7e-f).

Based on the good hydrogen evolution activity and pollutant removal performance of ZIS@CCS, we further selected different quinolone antibiotics OFL (Ofloxacin), LOM (Lomefloxacin), CIP (Ciprofloxacin), NOR (Norfloxacin), and ENR (Enrofloxacin) as common organic pollutants to study simultaneous photocatalytic hydrogen production and organic pollutant degradation. When NOR and ENR were added to the photocatalytic system, there was no significant change in the hydrogen evolution rate. On the contrary, the addition of OFL, LOM, and CIP in the photocatalytic system significantly improved the hydrogen evolution rate (Fig. 8a-b). At the same time, the 4-h removal efficiencies of OFL, LOM, and CIP were 89.4 %, 99.3 %, and 95.7 %, respectively (Fig. 8c-d). Under the condition of OFL, ZIS@CCS showed the highest hydrogen evolution rate, which was 0.32 mmol·g⁻¹·h⁻¹. Quinolone antibiotics exhibit slight variations in their physicochemical properties and chemical molecular structures, which strongly influences the photocatalytic degradation rate and, consequently, the hydrogen production rate [66]. Moreover, photocatalytic hydrogen production in synergy with organic degradation occurs within a bidirectional reactive system where different photocatalysts and pollutants need to be compatible to achieve optimal results [67].

In comparison with published literature, especially studies using ZnIn₂S₄ as the main catalyst, the hydrogen evolution rate of ZIS@CCS proposed in this paper is obviously higher, and its ability to obtain hydrogen from wastewater is also stronger. Moreover, the removal efficiency of the pollutant OFL is also remarkable (Fig. 8e, Table S3). Therefore, in the subsequent photocatalytic hydrogen production

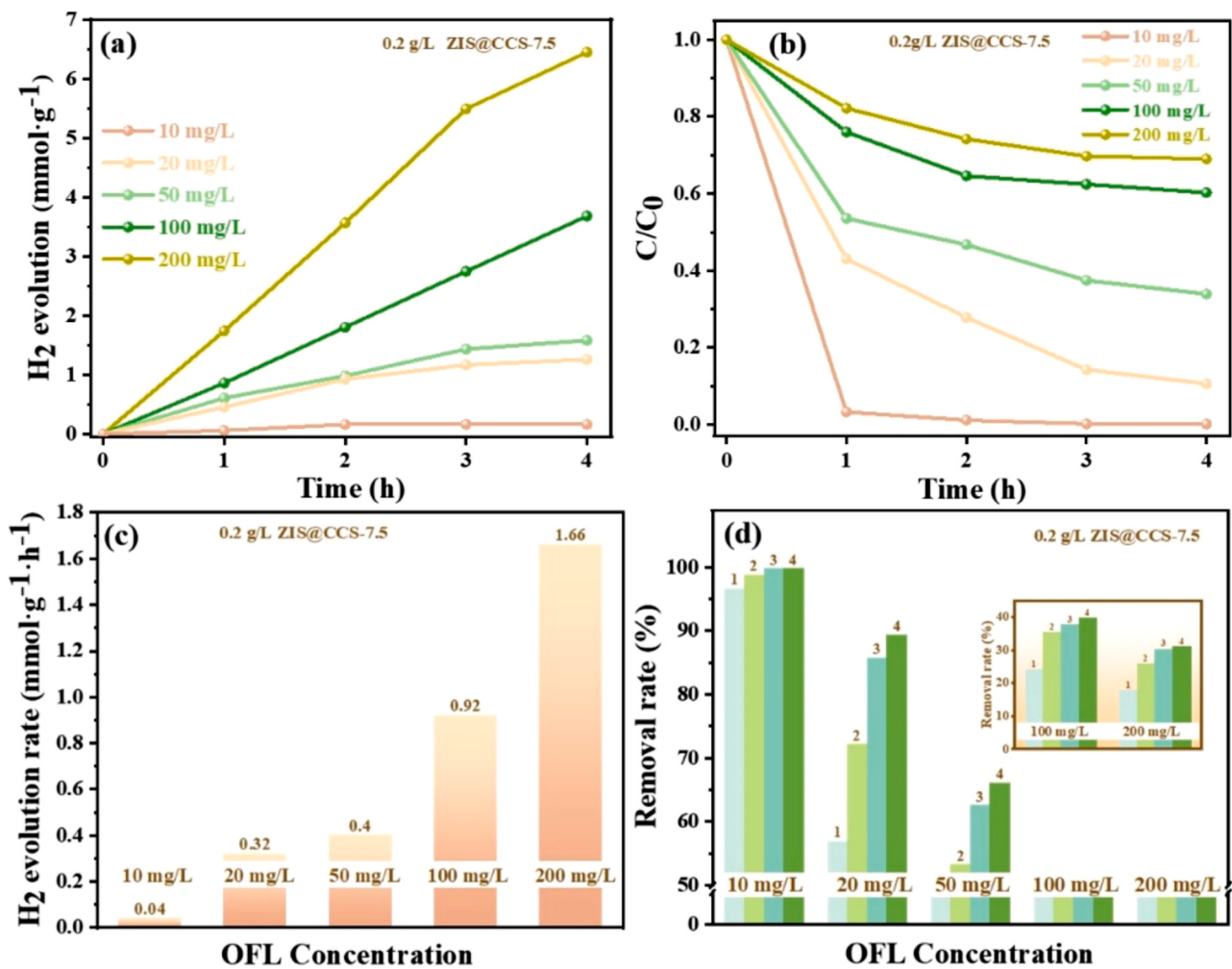


Fig. 10. Simultaneous photocatalytic H₂ evolution rate and the degradation efficiency of OFL containing different concentrations of OFL.

experiments, we chose OFL as a simulated pollutant to replace the sacrificial agent.

To explore the influence of the concentration of ZIS@CCS on the hydrogen evolution rate and pollutant removal efficiency, we designed gradient experiments with catalyst concentrations of 0.1 g/L, 0.2 g/L, 0.5 g/L, 1.0 g/L, and 2.0 g/L using 20 g/L OFL as the antibiotic wastewater. The experiments showed that the hydrogen evolution rate was highest at a catalyst concentration of 0.5 g/L, reaching 0.36 mmol·g⁻¹·h⁻¹. Increasing the catalyst concentration would result in a decrease in the hydrogen evolution rate (Fig. 9a-b). This is because that a high concentration of catalysts affects the diffusion of reactants to some extent and leads to an uneven distribution of active components inside the catalyst. Excess catalysts are prone to agglomeration, thereby reducing the specific surface area of the catalyst. In addition, as the catalyst concentration increases, the removal efficiency of OFL also increases (Fig. 9c-d). When the catalyst concentration reaches 1.0 g/L, the removal efficiency is close to 100 %. However, from the perspective of economic and environmental benefits, significantly increasing the catalyst concentration does not result in a significant improvement in the hydrogen evolution rate or pollutant removal efficiency. Therefore, selecting a catalyst concentration of 0.2 g/L is the most suitable choice.

Furthermore, to further explore the effect of OFL concentration on the hydrogen evolution rate and removal efficiency, we designed gradient experiments with OFL concentrations of 10 mg/L, 20 mg/L, 50 mg/L, 100 mg/L, and 200 mg/L using 0.2 g/L ZIS@CCS as the catalyst. The results showed that ZIS@CCS had a lower hydrogen evolution rate at low OFL concentrations (10 mg/L, 20 mg/L, 50 mg/L) and

tended to reach a balance. While at high concentrations (100 mg/L, 200 mg/L), it showed a long-term promotion effect on hydrogen evolution (Fig. 10a-b). After quantifying the hydrogen evolution rate, the hydrogen evolution rate of ZIS@CCS at high concentrations was about 5 times higher than that at low concentrations. When pollutants act as sacrificial agents, sufficient pollutants enable the catalyst to consume the photogenerated holes during pollutant degradation, thereby promoting the separation of photoinduced charge carriers and facilitating the hydrogen production reaction [68]. This is analogous to using a low concentration of a sacrificial agent. In addition, as the pollutant concentration increased, the removal efficiency gradually decreased, indicating that a certain amount of catalyst could only remove limited pollutants. Besides, compared with the initial pollutant concentration, the removal efficiency decreased (Fig. 10c-d).

3.4. Photocatalytic mechanism

The main active species in the photocatalytic system were revealed by ESR analysis. After the addition of DMPO, no ESR signal was detected in the dark, while typical signals of superoxide radicals and hydroxyl radicals were observed for the ZIS@CCS composite material in Fig. 11a-b after illumination. The weak signal appeared at 5 min and intensified at 10 min [14], with the peak intensity increasing with increasing illumination time. This indicates that active species are continuously generated over time under light and can be retained for a long time, continuing to play a role in the photocatalytic process and participating in the degradation of pollutants. It also suggests that the CB and VB of

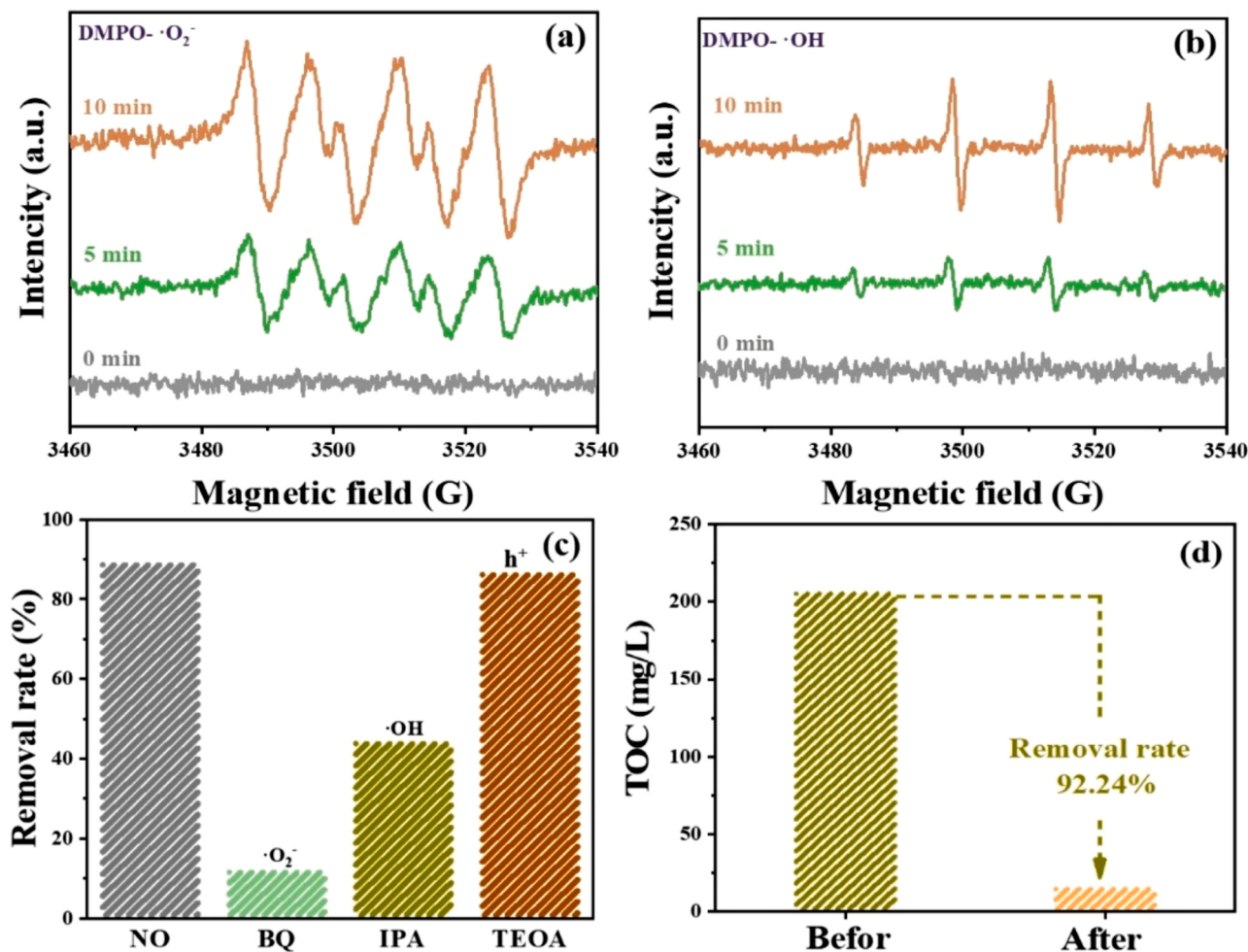


Fig. 11. DMPO spin-rapping ESR spectra of (a) DMPO-·O₂⁻ and (b) DMPO-·OH on ZIS@CCS; (c) Degradation efficiency of OFL over ZIS@CCS in the presence of different radical quenchers; (d) The removal rate of TOC from the simulated wastewater containing OFL.

the composite material have reached the conditions for generating ·O₂ and ·OH, respectively. The mechanism of OFL degradation by ZIS@CCS in the coupled system was explored through the capture experiments of free radicals (-O₂⁻, ·OH, and h⁺). BQ, IPA, and TEOA were chosen as scavengers of ·O₂, ·OH, and h⁺, respectively [69]. As shown in Fig. 11c and Fig. S7, the photocatalytic degradation of OFL was significantly inhibited by the addition of BQ and IPA. However, the addition of TEOA did not inhibit the photocatalytic degradation performance. This indicates that the removal of OFL mainly relies on ·O₂ and ·OH, or both oxidation species. Fig. 11d determines the degree of mineralization of organic pollutants by measuring the total organic carbon (TOC) concentration before and after the reaction in the OFL solution. The results showed a 92.24 % decrease in TOC concentration after a 4-h reaction, indicating that the majority of organic substances had been mineralized and converted into CO₂, achieving the goal of effective pollutant removal.

Fig. 12a-b and Fig. S8 illustrate the degradation pathway of OFL, combined with the identification of major intermediates using LC-MS. Hydroxylation was the first step, which results in an intermediate product (*m/z* = 391.0705), followed by dehydroxylation to remove two hydroxyl groups and obtain a product (*m/z* = 302.6741). Then, removal of the pyrimidine group and the triazine group led to two intermediate products with *m/z* values of 218.9665 and 177.9412, respectively. Subsequently, defluorination resulted in an intermediate product (*m/z* = 150.1079). Finally, pyridine removal, deamination, and hydroxylation furnished an intermediate product with *m/z* = 150.0037. Carbon dioxide, water, and some small organic molecules were produced

through further oxidation of the intermediates.

Referring to the band positions and bandgap widths in Fig. 5, we can plot the energy level diagrams (Fig. 12c) for the VB and CB of ZIS and CCS. The interaction between a few atomic layers at the interface of the contact between ZnIn₂S₄ and CuCo₂S₄ leads to changes in chemical bonding, which is supported by DFT calculations. They still maintain their respective crystal structures and band structures because their Fermi energy levels located at different position [70]. According to Fig. 5c-d, ZIS is an n-type semiconductor with the Fermi level close to the CB, while CCS is a p-type semiconductor with the Fermi level close to the VB. Due to the chemical bonding between the surface atomic layers of ZnIn₂S₄ and CuCo₂S₄, it is equivalent to a partial “doping” of both intrinsic semiconductors on the surface, resulting in the migration of charge carriers [71]. When the n-type ZIS contacts with the p-type CCS, the large difference in Fermi levels between them facilitates the transfer of carriers in opposite directions until the two Fermi levels are balanced [72]. Due to the carrier migration at the interface, an internal electric field can be formed when the p-type and n-type semiconductors combine to form a heterojunction. Meanwhile, during the diffusion process, electrons flow from the higher Fermi energy level of the n-type region to the lower Fermi energy level of the p-type region, while holes flow from the p-type region to the n-type region, thus causing the band structure to bend in the opposite direction until the Fermi energy levels reaching an equilibrium. Subsequently, positive holes will appear on the surface of the n-type conductor, while negative electrons will appear on the surface of the p-type conductor [73]. Due to the internal field at the interface, the photoinduced electrons transfer from the CB of CCS to the CB of ZIS,

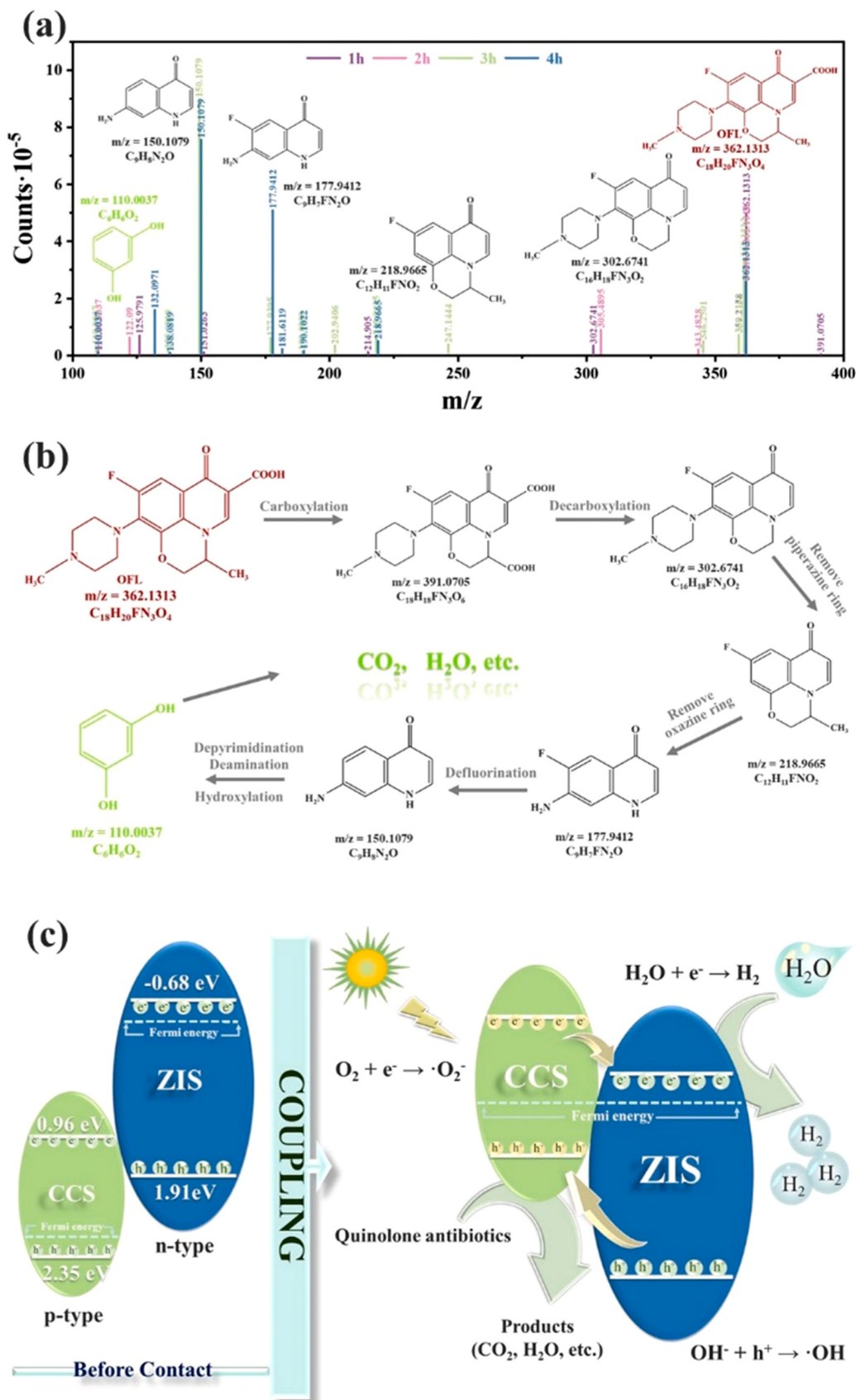


Fig. 12. (a-b) Pathway and main intermediates during the OFL degradation process; (c) Schematic illustration for photocatalytic hydrogen recovery from the antibiotic-over-p-n heterojunction ZIS@CCS system.

while the photoinduced holes of ZIS migrate to the VB of CCS. In this way, the photoinduced electrons and holes of ZIS and CCS can be effectively separated [74]. The accumulated electrons in the CB of ZIS can directly reduce H^+ in water to H_2 . Moreover, due to the CB position reaching the condition for generating O_2 , the electrons in the CB can also generate O_2 reactive species from oxygen in water. On the other hand, OFL acts as a sacrificial agent and consumes the remaining holes in the VB of CCS. Meanwhile, the holes combine with OH^- in water to generate OH , further promoting the separation of electron-hole pairs and completing the photocatalytic degradation process through the involvement of O_2 and OH . The construction of heterojunctions is a key method for effectively separating photoinduced carriers. The p-n heterojunction system formed between ZIS and CCS can facilitate the separation of photoinduced carriers and create different positions for reduction and oxidation reactions, thereby achieving photocatalytic hydrogen production and OFL removal.

4. Conclusions

In summary, this study employed a simple hydrothermal and oil bath approach to create a novel and efficient ZIS@CCS composite material to realize the dual objectives of simultaneous photodegradation of organic pollutants and hydrogen production. Cluster-like CCS was well dispersed and tight contact to ZIS, thus forming a p-n heterojunction. This facilitated the efficient separation of photo-generated electrons and holes. ZIS@CCS exhibited excellent hydrogen evolution activity, stability and recyclability in sacrificial agent-assisted photocatalysis. Additionally, it retained considerable hydrogen production rate as well as photodegradation activity in quinolone-type antibiotic wastewater. By coupling photocatalytic hydrogen production with organic pollutant degradation, clean hydrogen energy can be obtained without the consumption of expensive and toxic sacrificial agents. This work exhibits a new avenue for the design of dual-function photocatalysts, synergistic energy development, and environmental protection.

CRediT authorship contribution statement

Ruobing Wang: Conceptualization, Methodology, Investigation, Writing-original draft. **Weili Yu:** Methodology, Investigation. **Ningjie Fang:** Conceptualization, Supervision, Writing-review & editing. **Peng Wang:** DFT calculations. **Yinghao Chu:** Resources, Supervision, Validation. **Shilin Wu:** Investigation, Methodology. **Juan Liang:** Investigation, Methodology, Discussion.

Declaration of Competing Interest

The authors declare that they have no known competing financial interests or personal relationships that could have appeared to influence the work reported in this paper.

Data availability

Data will be made available on request.

Acknowledgments

This work was supported by the Projects of the Science and Technology Department of Sichuan Province (2023NSFSC0841), the Sichuan University Postdoctoral Interdisciplinary Innovation Fund (JCKX2208), and the Fundamental Research Funds for the Central Universities (2023SCU12099).

Appendix A. Supporting information

Supplementary data associated with this article can be found in the online version at [doi:10.1016/j.apcatb.2023.123284](https://doi.org/10.1016/j.apcatb.2023.123284).

References

- [1] Y. Li, Y. Fu, M. Zhu, Green synthesis of 3D tripyramid TiO_2 architectures with assistance of aloe extracts for highly efficient photocatalytic degradation of antibiotic ciprofloxacin, *Appl. Catal. B-Environ.* 260 (2020), 118149, <https://doi.org/10.1016/j.apcatb.2019.118149>.
- [2] M. Zhang, Y. Zhang, Y. Zhu, J. Wang, L. Qiao, Y. Zhao, Y. Tao, Y. Xiao, L. Tang, Insights into adsorption and high photocatalytic oxidation of ciprofloxacin under visible light by intra-molecular donor-acceptor like p-n isotype heterojunction: performance and mechanism, *Chem. Eng. J.* 464 (2023), 142533, <https://doi.org/10.1016/j.cej.2023.142533>.
- [3] Z. Shan, F. Ma, M. Xu, X. Shan, L. Shan, C. Cui, H. Guo, Kinetics and mechanism of enhanced norfloxacin degradation by $Fe_3O_4@La-BiFeO_3$ based on weak magnetization and efficient charge separation, *Chem. Eng. J.* 466 (2023), 143229, <https://doi.org/10.1016/j.cej.2023.143229>.
- [4] B. Wang, Z. Li, H. Ma, J. Zhang, L. Jiao, H. Hao, E. Liu, L. Xu, C. Wang, B. Zhou, X. Ma, Dynamic construction of self-assembled supramolecular $H_2SubPcB-OPhCOOH/Ag_3PO_4$ S-scheme arrays for visible photocatalytic oxidation of antibiotics, *Appl. Catal. B-Environ.* 318 (2022), 121882, <https://doi.org/10.1016/j.apcatb.2022.121882>.
- [5] Y. Chen, C. Jiang, Y. Wang, R. Song, Y. Tan, Y. Yang, Z. Zhang, Sources, environmental fate, and ecological risks of antibiotics in sediments of Asia's longest river: a whole-basin investigation, *Environ. Sci. Technol.* 56 (2022) 14439–14451, <https://doi.org/10.1021/acs.est.2c03413>.
- [6] H. Fang, A.S. Oberoi, Z. He, S.K. Khanal, H. Lu, Ciprofloxacin-degrading *paraclostridium* sp. isolated from sulfate-reducing bacteria-enriched sludge: optimization and mechanism, *Water Res.* 191 (2021), 116808, <https://doi.org/10.1016/j.watres.2021.116808>.
- [7] B.C. Hodges, E.L. Cates, J.-H. Kim, Challenges and prospects of advanced oxidation water treatment processes using catalytic nanomaterials, *Nat. Nanotechnol.* 13 (2018) 642–650, <https://doi.org/10.1038/s41565-018-0216-x>.
- [8] D.W. Wakerley, M.F. Kuehnle, K.L. Orchard, K.H. Ly, T.E. Rosser, E. Reisner, Solar-driven reforming of lignocellulose to H_2 with a $CdS/CdOx$ photocatalyst, *Nat. Energy* 2 (2017), 17021, <https://doi.org/10.1038/nenergy.2017.21>.
- [9] M. Ashraf, N. Ullah, I. Khan, W. Tremel, S. Ahmad, M.N. Tahir, Photoreforming of waste polymers for sustainable hydrogen fuel and chemicals feedstock: waste to energy, *Chem. Rev.* 123 (2023) 4443–4509, <https://doi.org/10.1021/acs.chemrev.2c00602>.
- [10] C. Bie, L. Wang, J. Yu, Challenges for photocatalytic overall water splitting, *Chem* 8 (2022) 1567–1574, <https://doi.org/10.1016/j.chempr.2022.04.013>.
- [11] K. Liu, L. Wang, T. Fu, H. Zhang, C. Lu, Z. Tong, Y. Yang, Y. Peng, Oxygen-functionalized Ti_3C_2 MXene/exfoliated montmorillonite supported S-scheme $BiOBr/Bi_2MoO_6$ heterostructures for efficient photocatalytic quinolone antibiotics degradation, *Chem. Eng. J.* 457 (2023), 141271, <https://doi.org/10.1016/j.cej.2023.141271>.
- [12] F. Wang, Y. Feng, P. Chen, Y. Wang, Y. Su, Q. Zhang, Y. Zeng, Z. Xie, H. Liu, Y. Liu, W. Lv, G. Liu, Photocatalytic degradation of fluoroquinolone antibiotics using ordered mesoporous $g-C_3N_4$ under simulated sunlight irradiation: kinetics, mechanism, and antibacterial activity elimination, *Appl. Catal. B-Environ.* 227 (2018) 114–122, <https://doi.org/10.1016/j.apcatb.2018.01.024>.
- [13] H. Mai, D. Chen, Y. Tachibana, H. Suzuki, R. Abe, R.A. Caruso, Developing sustainable, high-performance perovskites in photocatalysis: design strategies and applications, *Chem. Soc. Rev.* 50 (2021) 13692–13729, <https://doi.org/10.1039/DICS00684C>.
- [14] S. Zhang, G. Hu, M. Chen, B. Li, W. Dai, F. Deng, L. Yang, J. Zou, S. Luo, Interfacial oxygen vacancy modulated $Ag_3PO_4 @MoS_2$ Z-scheme system for efficient photocatalytic hydrogen recovery from antibiotic wastewater, *Appl. Catal. B-Environ.* 330 (2023), 122584, <https://doi.org/10.1016/j.apcatb.2023.122584>.
- [15] S. Liu, X. Zhou, C. Yang, C. Wei, Y. Hu, Cu atoms on $UiO-66-NH_2/ZnIn_2S_4$ nanosheets enhance photocatalytic performance for recovering hydrogen energy from organic wastewater treatment, *Appl. Catal. B-Environ.* 330 (2023), <https://doi.org/10.1016/j.apcatb.2023.122572>.
- [16] C. Zhu, L. Lu, J. Xu, S. Song, Q. Fang, R. Liu, Y. Shen, J. Zhao, W. Dong, Y. Shen, Metal monovacancy-induced spin polarization for simultaneous energy recovery and wastewater purification, *Chem. Eng. J.* 451 (2023), 138537, <https://doi.org/10.1016/j.cej.2022.138537>.
- [17] J. Tang, X. Liu, Y. Liu, X. Zhang, Y. Lin, L. Chen, D. Fang, J. Wang, Novel Z-scheme $Sr_2MgSi_2O_7:Eu^{2+}, Dy^{3+}/Ag_3PO_4$ photocatalyst for round-the-clock efficient degradation of organic pollutants and hydrogen production, *Chem. Eng. J.* 435 (2022), 134773, <https://doi.org/10.1016/j.cej.2022.134773>.
- [18] K. Li, Y. Cai, X. Yang, S. Wang, C. Teng, Y. Tian, Q. Min, W. Zhu, H_2S involved photocatalytic system: a novel syngas production strategy by boosting the photoreduction of CO_2 while recovering hydrogen from the environmental toxicant, *Adv. Funct. Mater.* 32 (2022), <https://doi.org/10.1002/adfm.202113002>.
- [19] P. Wang, S. Fan, X. Li, J. Wang, Z. Liu, Z. Niu, M.O. Tadé, S. Liu, Single Pd atoms synergistically manipulating charge polarization and active sites for simultaneously photocatalytic hydrogen production and oxidation of benzylamine, *Nano Energy* 95 (2022), 107045, <https://doi.org/10.1016/j.nanoen.2022.107045>.
- [20] P. Jin, L. Wang, X. Ma, R. Lian, J. Huang, H. She, M. Zhang, Q. Wang, Construction of hierarchical $ZnIn_2S_4@PCN-224$ heterojunction for boosting photocatalytic performance in hydrogen production and degradation of tetracycline hydrochloride, *Appl. Catal. B-Environ.* 284 (2021), <https://doi.org/10.1016/j.apcatb.2020.119762>.

[21] T. Lange, S. Reichenberger, S. Ristig, M. Rohe, J. Strunk, S. Barcikowski, R. Schlögl, Zinc sulfide for photocatalysis: White angel or black sheep? *Prog. Mater. Sci.* 124 (2022), 100865 <https://doi.org/10.1016/j.pmatsci.2021.100865>.

[22] X. Tao, H. Zhou, C. Zhang, N. Ta, R. Li, C. Li, Triclinic-phase bismuth chromate: a promising candidate for photocatalytic water splitting with broad spectrum ranges, *Adv. Mater.* 35 (2023), e2211182, <https://doi.org/10.1002/adma.202211182>.

[23] J. Zhang, Y. Pan, D. Feng, L. Cui, S. Zhao, J. Hu, S. Wang, Y. Qin, Mechanistic insight into the synergy between platinum single atom and cluster dual active sites boosting photocatalytic hydrogen evolution, *Adv. Mater.* (2023), e2300902, <https://doi.org/10.1002/adma.202300902>.

[24] C. Wu, W. Huang, H. Liu, K. Lv, Q. Li, Insight into synergistic effect of Ti_3C_2 MXene and MoS_2 on anti-photo-corrosion and photocatalytic of CdS for hydrogen production, *Appl. Catal. B-Environ.* 330 (2023), 122653, <https://doi.org/10.1016/j.apcatb.2023.122653>.

[25] A. Jiang, H. Guo, S. Yu, F. Zhang, T. Shuai, Y. Ke, P. Yang, Y. Zhou, Dual charge-accepting engineering modified $AgIn_5S_8/CdS$ quantum dots for efficient photocatalytic hydrogen evolution overall H_2S splitting, *Appl. Catal. B-Environ.* 332 (2023), 122747, <https://doi.org/10.1016/j.apcatb.2023.122747>.

[26] Y. Zhang, Y. Li, X. Xin, Y. Wang, P. Guo, R. Wang, B. Wang, W. Huang, A. J. Sobrido, X. Li, Internal quantum efficiency higher than 100% achieved by combining doping and quantum effects for photocatalytic overall water splitting, *Nat. Energy* (2023), <https://doi.org/10.1038/s41560-023-01242-7>.

[27] Y. Su, Z. Wei, Y. Lian, Q. Mu, W. Pan, D. Song, Y. Qin, W. Hua, J. Cheng, Z. Deng, Y. Peng, Defect-driven electroless deposition and activation of platinum sites on $ZnIn_2S_4$ nanosheets for accelerated kinetics of photocatalytic hydrogen production, *Appl. Catal. B-Environ.* (2023), 122827, <https://doi.org/10.1016/j.apcatb.2023.122827>.

[28] J. Xu, W. Zhong, F. Chen, X. Wang, H. Yu, In situ cascade growth-induced strong coupling effect toward efficient photocatalytic hydrogen evolution of $ReS_2/ZnIn_2S_4$, *Appl. Catal. B-Environ.* 328 (2023), 122493, <https://doi.org/10.1016/j.apcatb.2023.122493>.

[29] Y. Zhong, M. Li, X. Luan, F. Gao, H. Wu, J. Zi, Z. Lian, Ultrathin $ZnIn_2S_4/ZnSe$ heteronanosheets with modulated S-scheme enable high efficiency of visible-light-responsive photocatalytic hydrogen evolution, *Appl. Catal. B-Environ.* (2023), 122859, <https://doi.org/10.1016/j.apcatb.2023.122859>.

[30] Y. Shi, L. Li, Z. Xu, F. Guo, W. Shi, Construction of full solar-spectrum available S-scheme heterojunction for boosted photothermal-assisted photocatalytic H_2 production, *Chem. Eng. J.* 459 (2023), 141549, <https://doi.org/10.1016/j.cej.2023.141549>.

[31] G. Zhang, S. Huang, X. Li, D. Chen, N. Li, Q. Xu, H. Li, J. Lu, Internal electric field engineering of bifunctional 2D/2D heterojunction photocatalyst for cooperative H_2 production and alcohol conversion, *Appl. Catal. B-Environ.* 331 (2023), 122725, <https://doi.org/10.1016/j.apcatb.2023.122725>.

[32] X. Zheng, Y. Song, Y. Liu, Y. Yang, D. Wu, Y. Yang, S. Feng, J. Li, W. Liu, Y. Shen, X. Tian, $ZnIn_2S_4$ -based photocatalysts for photocatalytic hydrogen evolution via water splitting, in: *Coord. Chem. Rev.*, 475, 2023, 214898, <https://doi.org/10.1016/j.ccr.2022.214898>.

[33] Y. Yang, S. Zhao, F. Bi, J. Chen, Y. Wang, L. Cui, J. Xu, X. Zhang, Highly efficient photothermal catalysis of toluene over Co_3O_4/TiO_2 p-n heterojunction: The crucial roles of interface defects and band structure, *Appl. Catal. B-Environ.* 315 (2022), 121550, <https://doi.org/10.1016/j.apcatb.2022.121550>.

[34] W. He, L. Liu, T. Ma, H. Han, J. Zhu, Y. Liu, Z. Fang, Z. Yang, K. Guo, Controllable morphology $Cofe_{2}O_4/g-C_3N_4$ p-n heterojunction photocatalysts with built-in electric field enhance photocatalytic performance, *Appl. Catal. B-Environ.* 306 (2022), 121107, <https://doi.org/10.1016/j.apcatb.2022.121107>.

[35] J. Niu, R. Hu, L. Tang, Y. Huang, J. Cheng, Y. Hu, In-situ growth of C-F@CCS@ZIF8/67-1/1 photocatalysts with internal electric field and interfacial enhancement on cobalt-copper foam surface for simultaneous removal of ciprofloxacin and Cr(VI), *Appl. Catal. B-Environ.* 334 (2023), 122857, <https://doi.org/10.1016/j.apcatb.2023.122857>.

[36] M. Chauhan, K. Soni, P.E. Karthik, K.P. Reddy, C.S. Gopinath, S. Deka, Promising visible-light driven hydrogen production from water on a highly efficient $CuCo_2S_4$ nanosheet photocatalyst, *J. Mater. Chem. A* 7 (2019) 6985–6994, <https://doi.org/10.1039/c9ta00391f>.

[37] X. Feng, L. Zhang, Engineering yolk-shell $CuCo_2S_4@Cu_2O$ Z-scheme nanoreactors for accelerating generation of value-added chemicals and of degradation multi-organic contaminants, *J. Mater. Sci. Technol.* 156 (2023) 54–63, <https://doi.org/10.1016/j.jmst.2022.09.040>.

[38] X. Yang, M.D. Hesami, E. Nazemipool, A. Bahadoran, M. Al-Bahrani, B. Azizi, Fabrication of $CuCo_2S_4$ yolk-shell spheres embedded with S-scheme V_2O_5 -deposited on wrinkled $g-C_3N_4$ for effective promotion of levofloxacin photodegradation, *Sep. Purif. Technol.* 301 (2022), 122005, <https://doi.org/10.1016/j.seppur.2022.122005>.

[39] Y. Wang, C. Yang, K. Zhang, L. Guo, R. Li, A. Zaheer, F. Fu, B. Xu, D. Wang, In-situ construction of 2D/2D $CuCo_2S_4/Bi_2WO_6$ contact heterojunction as a visible-light-driven fenton-like catalyst with highly efficient charge transfer for highly efficient degradation of tetracycline hydrochloride, *Colloids Surf. Physicochem. Eng. Asp.* 634 (2022), <https://doi.org/10.1016/j.colsurfa.2021.127965>.

[40] S. Cao, L. Piao, Considerations for a more accurate evaluation method for photocatalytic water splitting, *Angew. Chem. Int. Ed.* 59 (2020) 18312–18320, <https://doi.org/10.1002/anie.202009633>.

[41] D. Zeng, Z. Lu, X. Gao, B. Wu, W.-J. Ong, Hierarchical flower-like $ZnIn_2S_4$ anchored with well-dispersed Ni_1P_5 nanoparticles for high-quantum-yield photocatalytic H_2 evolution under visible light, *Catal. Sci. Technol.* 9 (2019) 4010–4016, <https://doi.org/10.1039/c9tc00901a>.

[42] G. Kresse, J. Furthmüller, Efficiency of ab-initio total energy calculations for metals and semiconductors using a plane-wave basis set, *Comput. Mater. Sci.* 6 (1996) 15–50, [https://doi.org/10.1016/0927-0256\(96\)00008-0](https://doi.org/10.1016/0927-0256(96)00008-0).

[43] X. Shi, C. Dai, X. Wang, J. Hu, J. Zhang, L. Zheng, L. Mao, H. Zheng, M. Zhu, Protruding Pt single-sites on hexagonal $ZnIn_2S_4$ to accelerate photocatalytic hydrogen evolution, *Nat. Commun.* 13 (2022) 1287, <https://doi.org/10.1038/s41467-022-28995-1>.

[44] Y. Su, Z. Wei, Y. Lian, Q. Mu, W. Pan, D. Song, Y. Qin, W. Hua, J. Cheng, Z. Deng, Y. Peng, Defect-driven electroless deposition and activation of platinum sites on $ZnIn_2S_4$ nanosheets for accelerated kinetics of photocatalytic hydrogen production, *Appl. Catal. B-Environ.* 334 (2023), 122827, <https://doi.org/10.1016/j.apcatb.2023.122827>.

[45] F. Hasanvandian, M. Zehtab Salmasi, M. Moradi, S. Farshineh Saei, B. Kakavandi, S. Rahman Setayesh, Enhanced spatially coupling heterojunction assembled from $CuCo_2S_4$ yolk-shell hollow sphere encapsulated by Bi-modified TiO_2 for highly efficient CO_2 photoreduction, *Chem. Eng. J.* 444 (2022), 136493, <https://doi.org/10.1016/j.cej.2022.136493>.

[46] K. Zhang, M. Dan, J. Yang, F. Wu, L. Wang, H. Tang, Z.Q. Liu, Surface energy mediated sulfur vacancy of $ZnIn_2S_4$ atomic layers for photocatalytic H_2O_2 production, *Adv. Funct. Mater.* (2023), <https://doi.org/10.1002/adfm.202302964>.

[47] Y. Zhong, M. Li, X. Luan, F. Gao, H. Wu, J. Zi, Z. Lian, Ultrathin $ZnIn_2S_4/ZnSe$ heteronanosheets with modulated S-scheme enable high efficiency of visible-light-responsive photocatalytic hydrogen evolution, *Appl. Catal. B-Environ.* 335 (2023), 122859, <https://doi.org/10.1016/j.apcatb.2023.122859>.

[48] L. Ye, J. Fu, Z. Xu, R. Yuan, Z. Li, Facile one-pot solvothermal method to synthesize sheet-on-sheet reduced graphene oxide (RGO)/ $ZnIn_2S_4$ nanocomposites with superior photocatalytic performance, *ACS Appl. Mater. Interfaces* 6 (2014) 3483–3490, <https://doi.org/10.1021/am5004415>.

[49] M. Mehmandoust, F. Uzcan, M. Soylak, N. Erk, Dual-response electrochemical electrode for sensitive monitoring of topotecan and mitomycin as anticancer drugs in real samples, *Chemosphere* 291 (2022), 132809, <https://doi.org/10.1016/j.chemosphere.2021.132809>.

[50] J. Wang, D. Wang, X. Zhang, C. Zhao, M. Zhang, Z. Zhang, J. Wang, An anti-symmetric dual (ASD) Z-scheme photocatalytic system: $(ZnIn_2S_4/Er^{3+}:Y_3Al_5O_{12} @ ZnTiO_3/Caln_2S_4)$ for organic pollutants degradation with simultaneous hydrogen evolution, *Int. J. Hydrog. Energy* 44 (2019) 6592–6607, <https://doi.org/10.1016/j.ijhydene.2019.01.214>.

[51] S. Wu, H. Zhao, F. Dong, W. Ling, Z. Tang, J. Zhang, Construction of superhydrophobic Ru/TiCeO_x catalysts for the enhanced water resistance of o-dichlorobenzene catalytic combustion, *ACS Appl. Mater. Interfaces* 13 (2021) 2610–2621, <https://doi.org/10.1021/acsami.0c18636>.

[52] S.S.M. Bhat, S.A. Pawar, D. Potphode, C.-K. Moon, J.M. Suh, C. Kim, S. Choi, D. S. Patil, J.-J. Kim, J.C. Shin, H.W. Jang, Substantially enhanced photoelectrochemical performance of TiO_2 nanorods/ CdS nanocrystals heterojunction photoanode decorated with MoS_2 nanosheets, *Appl. Catal. B-Environ.* 259 (2019), 118102, <https://doi.org/10.1016/j.apcatb.2019.118102>.

[53] K.H. Rahman, A.K. Kar, Effect of band gap variation and sensitization process of polyaniline (PANI)- TiO_2 p-n heterojunction photocatalysts on the enhancement of photocatalytic degradation of toxic methylene blue with UV irradiation, *J. Environ. Chem. Eng.* 8 (2020), 104181, <https://doi.org/10.1016/j.jece.2020.104181>.

[54] H. Zhao, S. Cui, L. Yang, G. Li, N. Li, X. Li, Synthesis of hierarchically meso-macroporous TiO_2/CdS heterojunction photocatalysts with excellent visible-light photocatalytic activity, *J. Colloid Interface Sci.* 512 (2018) 47–54, <https://doi.org/10.1016/j.jcis.2017.10.011>.

[55] J.Y. Li, C.L. Tan, M.Y. Qi, Z.R. Tang, Y.J. Xu, Exposed zinc sites on hybrid $ZnIn_2S_4@CdS$ nanocages for efficient regioselective photocatalytic epoxide alcoholysis, *Angew. Chem. Int. Ed. Engl.* 62 (2023), e202303054, <https://doi.org/10.1002/anie.202303054>.

[56] W.-J. Ong, L.K. Putri, Y.-C. Tan, L.-L. Tan, N. Li, Y.H. Ng, X. Wen, S.-P. Chai, Unravelling charge carrier dynamics in protonated $g-C_3N_4$ interfaced with carbon nanodots as co-catalysts toward enhanced photocatalytic CO_2 reduction: a combined experimental and first-principles DFT study, *Nano Res.* 10 (2017) 1673–1696, <https://doi.org/10.1007/s12274-016-1391-4>.

[57] Y. Cui, X. Zhang, R. Guo, H. Zhang, B. Li, M. Xie, Q. Cheng, X. Cheng, Construction of $Bi_2O_3/g-C_3N_4$ composite photocatalyst and its enhanced visible light photocatalytic performance and mechanism, *Sep. Purif. Technol.* 203 (2018) 301–309, <https://doi.org/10.1016/j.seppur.2018.04.061>.

[58] W. Yin, L. Bai, Y. Zhu, S. Zhong, L. Zhao, Z. Li, S. Bai, Embedding metal in the interface of a p-n heterojunction with a stack design for superior Z-scheme photocatalytic hydrogen evolution, *ACS Appl. Mater. Interfaces* 8 (2016) 23133–23142, <https://doi.org/10.1021/acsami.6b07754>.

[59] X. Shi, C. Dai, X. Wang, J. Hu, J. Zhang, L. Zheng, L. Mao, H. Zheng, M. Zhu, Protruding Pt single-sites on hexagonal $ZnIn_2S_4$ to accelerate photocatalytic hydrogen evolution, *Nat. Commun.* 13 (2022) 1287, <https://doi.org/10.1038/s41467-022-28995-1>.

[60] S. Zhang, Z. Zhang, Y. Si, B. Li, F. Deng, L. Yang, X. Liu, W. Dai, S. Luo, Gradient hydrogen migration modulated with self-adapting S vacancy in copper-doped $ZnIn_2S_4$ nanosheet for photocatalytic hydrogen evolution, *ACS Nano* 15 (2021) 15238–15248, <https://doi.org/10.1021/acsnano.1c05834>.

[61] C. Du, Q. Zhang, Z. Lin, B. Yan, C. Xia, G. Yang, Half-unit-cell $ZnIn_2S_4$ monolayer with sulfur vacancies for photocatalytic hydrogen evolution, *Appl. Catal. B-Environ.* 248 (2019) 193–201, <https://doi.org/10.1016/j.apcatb.2019.02.027>.

[62] X. Mao, Y. Wang, C. Xiang, D. Zhan, H. Zhang, E. Yan, F. Xu, X. Hu, J. Zhang, L. Sun, Y. Zou, Core-shell structured $CuCo_2S_4@CoMoO_4$ nanorods for advanced electrode materials, *J. Alloy. Compd.* 844 (2020), 156133, <https://doi.org/10.1016/j.jallcom.2020.156133>.

[63] Q. Luan, X. Xue, R. Li, L. Gu, W. Dong, D. Zhou, X. Wang, B. Li, G. Wang, C. Hou, Boosting photocatalytic hydrogen evolution: Orbital redistribution of ultrathin ZnIn₂S₄ nanosheets via atomic defects, *Appl. Catal. B-Environ.* 305 (2022), 121007, <https://doi.org/10.1016/j.apcatb.2021.121007>.

[64] Q. Zhang, H. Gu, X. Wang, L. Li, J. Zhang, H. Zhang, Y.-F. Li, W.-L. Dai, Robust hollow tubular ZnIn₂S₄ modified with embedded metal-organic-framework-layers: extraordinarily high photocatalytic hydrogen evolution activity under simulated and real sunlight irradiation, *Appl. Catal. B-Environ.* 298 (2021), 120632, <https://doi.org/10.1016/j.apcatb.2021.120632>.

[65] X. Shi, L. Mao, P. Yang, H. Zheng, M. Fujitsuka, J. Zhang, T. Majima, Ultrathin ZnIn₂S₄ nanosheets with active (110) facet exposure and efficient charge separation for cocatalyst free photocatalytic hydrogen evolution, *Appl. Catal. B-Environ.* 265 (2020), 118616, <https://doi.org/10.1016/j.apcatb.2020.118616>.

[66] S.E. Estrada-Flórez, E.A. Serna-Galvis, R.A. Torres-Palma, Photocatalytic vs. sonochemical removal of antibiotics in water: structure-degradability relationship, mineralization, antimicrobial activity, and matrix effects, *J. Environ. Chem. Eng.* 8 (2020), <https://doi.org/10.1016/j.jece.2020.104359>.

[67] Z. Yan, K. Yin, M. Xu, N. Fang, W. Yu, Y. Chu, S. Shu, Photocatalysis for synergistic water remediation and H₂ production: a review, *Chem. Eng. J.* 472 (2023), <https://doi.org/10.1016/j.cej.2023.145066>.

[68] C.R. López, E.P. Melián, J.A. Ortega Méndez, D.E. Santiago, J.M. Doña Rodríguez, O. González Díaz, Comparative study of alcohols as sacrificial agents in H₂ production by heterogeneous photocatalysis using Pt/TiO₂ catalysts, *J. Photochem. Photobiol. A: Chem.* 312 (2015) 45–54, <https://doi.org/10.1016/j.jphotochem.2015.07.005>.

[69] K. Wang, X. Shao, K. Zhang, J. Wang, X. Wu, H. Wang, 0D/3D Bi₃TaO₇/ZnIn₂S₄ heterojunction photocatalyst towards degradation of antibiotics coupled with simultaneous H₂ evolution: in situ irradiated XPS investigation and S-scheme mechanism insight, *Appl. Surf. Sci.* 596 (2022), <https://doi.org/10.1016/j.apsusc.2022.153444>.

[70] Y.-Y. Yang, H.-P. Feng, C.-G. Niu, D.-W. Huang, H. Guo, C. Liang, H.-Y. Liu, S. Chen, N. Tang, L. Li, Constructing a plasma-based Schottky heterojunction for near-infrared-driven photothermal synergistic water disinfection: synergistic effects and antibacterial mechanisms, *Chem. Eng. J.* 426 (2021), <https://doi.org/10.1016/j.cej.2021.131902>.

[71] H. Feng, J. Yu, J. Tang, L. Tang, Y. Liu, Y. Lu, J. Wang, T. Ni, Y. Yang, Y. Yi, Enhanced electro-oxidation performance of FeCoLDH to organic pollutants using hydrophilic structure, *J. Hazard. Mater.* 430 (2022), <https://doi.org/10.1016/j.jhazmat.2022.128464>.

[72] I. Hussain, M.Z. Ansari, C. Lamiel, T. Hussain, M.S. Javed, T. Kaewmaraya, M. Ahmad, N. Qin, K. Zhang, In situ grown heterostructure based on MOF-derived carbon containing n-type Zn-In-S and dry-oxidative p-type CuO as pseudocapacitive electrode materials, *ACS Energy Lett.* 8 (2023) 1887–1895, <https://doi.org/10.1021/acsenergylett.3c00221>.

[73] Q.-Q. Fan, C.-G. Niu, H. Guo, D.-W. Huang, Z.-T. Dong, Y.-Y. Yang, H.-Y. Liu, L. Li, M.-Z. Qin, Insights into the role of reactive oxygen species in photocatalytic H₂O₂ generation and OTC removal over a novel BN/ZnIn₂S₆ heterojunction, *J. Hazard. Mater.* 438 (2022), <https://doi.org/10.1016/j.jhazmat.2022.129483>.

[74] H. Feng, J. Yu, L. Tang, J. Wang, H. Dong, T. Ni, J. Tang, W. Tang, X. Zhu, C. Liang, Improved hydrogen evolution activity of layered double hydroxide by optimizing the electronic structure, *Appl. Catal. B-Environ.* 297 (2021), 120478, <https://doi.org/10.1016/j.apcatb.2021.120478>.